ESCORT: Efficient Stein-variational and Sliced Consistency-Optimized Temporal Belief Representation for POMDPs

Yunuo Zhang

Vanderbilt University yunuo.zhang@vanderbilt.edu

Baiting Luo

Vanderbilt University baiting.luo@vanderbilt.edu

Ayan Mukhopadhyay

Vanderbilt University ayan.mukhopadhyay@vanderbilt.edu

Gabor Karsai

Vanderbilt University gabor.karsai@vanderbilt.edu

Abhishek Dubev

Vanderbilt University abhishek.dubey@vanderbilt.edu

Abstract

In Partially Observable Markov Decision Processes (POMDPs), maintaining and updating belief distributions over possible underlying states provides a principled way to summarize action-observation history for effective decision-making under uncertainty. As environments grow more realistic, belief distributions develop complexity that standard mathematical models cannot accurately capture, creating a fundamental challenge in maintaining representational accuracy. Despite advances in deep learning and probabilistic modeling, existing POMDP belief approximation methods fail to accurately represent complex uncertainty structures such as high-dimensional, multi-modal belief distributions, resulting in estimation errors that lead to suboptimal agent behaviors. To address this challenge, we present ESCORT (Efficient Stein-variational and sliced Consistency-Optimized Representation for Temporal beliefs), a particle-based framework for capturing complex, multi-modal distributions in high-dimensional belief spaces. ESCORT extends SVGD with two key innovations: correlation-aware projections that model dependencies between state dimensions, and temporal consistency constraints that stabilize updates while preserving correlation structures. This approach retains SVGD's attractive-repulsive particle dynamics while enabling accurate modeling of intricate correlation patterns. Unlike particle filters prone to degeneracy or parametric methods with fixed representational capacity, ESCORT dynamically adapts to belief landscape complexity without resampling or restrictive distributional assumptions. We demonstrate ESCORT's effectiveness through extensive evaluations on both POMDP domains and synthetic multi-modal distributions of varying dimensionality, where it consistently outperforms state-of-theart methods in terms of belief approximation accuracy and downstream decision quality. Our code is available at https://github.com/scope-lab-vu/ESCORT.

1 Introduction

Partially Observable Markov Decision Processes (POMDPs) [Åström, 1965] provide a powerful mathematical framework for sequential decision-making under uncertainty, enabling agents to make optimal decisions despite having only partial information about their environment [Kaelbling et al., 1998]. At the core of POMDP solutions lies the concept of belief states: probability distributions over possible underlying states conditioned on the history of actions and observations [Kaelbling et al., 1998]. As POMDPs are applied to increasingly complex real-world domains [Lauri et al., 2023, Kurniawati, 2022, Zhang et al., 2024], the underlying belief distributions develop sophisticated characteristics that standard mathematical models struggle to accurately capture [Roy and Gordon, 2002, Brooks et al., 2006, Zhang et al., 2025]. Specifically, realistic belief distributions in POMDPs often exhibit a challenging combination of high dimensionality (due to complex state spaces) [Roy and Gordon, 2002] and multi-modality (from ambiguous observations creating multiple distinct hypotheses) [Chen et al., 2022, Zhang et al., 2025], which traditional approaches struggle to model efficiently. The inability to efficiently represent and update these complex belief distributions creates a fundamental bottleneck in developing practical POMDP solutions, as even small errors in belief approximation can propagate and significantly degrade decision quality over time.

Existing approaches to belief approximation in POMDPs face significant limitations with complex distributions. Parametric methods using neural representations struggle with uncertainty structures: DRQN [Hausknecht and Stone, 2015] and ADRQN [Zhu et al., 2018] compress histories into vectors that poorly capture multi-modal uncertainty, while even DVRL [Igl et al., 2018], despite using particle-based VAEs [Kingma and Welling, 2013], fails to maintain multiple distinct hypotheses simultaneously. These parametric approaches efficiently process high-dimensional data but sacrifice representational expressiveness—despite theoretical universal approximation power, neural networks face computational inefficiency and generalization challenges [Zhang et al., 2016]. Their fixed parametric nature prevents adaptation to varying uncertainty complexity, causing cumulative belief estimation errors over time.

On the other hand, particle-based methods offer flexibility in representing arbitrary distributions but face critical limitations. SIR filters [Gordon et al., 1993], which underpin leading POMDP solvers like POMCP [Silver and Veness, 2010], POMCPOW [Sunberg and Kochenderfer, 2018], ARDESPOT [Somani et al., 2013], and AdaOPS [Wu et al., 2021], struggle with the curse of dimensionality and particle degeneracy in high-dimensional spaces. Their stochastic resampling leads to mode collapse, failing to maintain coverage across multi-modal distributions, especially with ambiguous observations [Zhang et al., 2025]. These methods also inefficiently capture dependencies between state dimensions—either making oversimplified independence assumptions or requiring exponentially more particles to model joint distributions accurately, significantly limiting their applicability to complex POMDPs.

Inspired by the effectiveness of Stein Variational Gradient Descent (SVGD) [Liu, 2017] in Bayesian inference, we explore deterministic particle evolution as a principled alternative. SVGD avoids resampling-induced degeneracy through continuous gradient-based updates: particles move deterministically via $\nabla \log p(x)$ with kernel repulsion $\nabla k(x,x')$ maintaining multi-modal coverage without discarding hypotheses [Liu, 2017]. Unlike fixed parametric architectures, SVGD dynamically adapts its particle distribution—concentrating particles in high-uncertainty regions while providing sparse coverage elsewhere—aligning representational capacity with belief complexity without architectural changes. However, standard SVGD itself suffers from kernel degeneracy in highdimensional spaces [Zhuo et al., 2017, Chen and Ghattas, 2020]—weakening both attractive and repulsive forces—and cannot preserve complex correlation structures between state dimensions, leading to mode collapse in multi-modal distributions. Recent extensions like MP-SVGD [Zhuo et al., 2017] and SVMP [Wang et al., 2018] have demonstrated success in high-dimensional Bayesian inference by leveraging graphical model structures to guide particle evolution. However, these methods require fixed structures that cannot adapt to observation-dependent correlations in POMDPs, where belief correlation patterns change dynamically with observation history [Boyen and Koller, 1998].

ESCORT addresses these fundamental limitations through a novel belief update mechanism that extends SVGD with two key regularization components. Drawing insights from sliced optimal transport theory [Kolouri et al., 2019], we introduce: (1) a correlation-aware regularization that preserves dimensional dependencies during particle updates, mitigating kernel degeneracy while maintain-

ing multi-modal representational flexibility, and (2) a temporal consistency constraint that prevents unrealistic belief jumps between timesteps while preserving learned correlation structures. This deterministic update framework with targeted regularization prevents the accumulation of estimation errors that propagate through sequential decision-making. Our contributions are:

- We extend SVGD to overcome particle degeneracy in traditional filters and fixed representational capacity in parametric approaches for complex POMDP belief approximation.
- We introduce correlation-aware regularization inspired by optimal transport theory that preserves dimensional dependencies and mitigates kernel degeneracy in high-dimensional spaces.
- We develop temporal consistency regularization that prevents unrealistic belief jumps while preserving correlation structures, ensuring stable belief evolution.
- While future work will address computational overhead from correlation matrix computation and projection optimization, ESCORT provides a modular belief representation that seamlessly integrates with existing POMDP solvers for broader practical impact.
- We demonstrate ESCORT's effectiveness through extensive experiments on Light-Dark Navigation [Platt et al., 2010, Silver and Veness, 2010], Kidnapped Robot [Choset et al., 2005], and Multi-Target Tracking [Rong Li and Jilkov, 2003] benchmarks, as well as synthetic multi-modal distributions, showing consistent improvements in belief fidelity and decision quality.

2 Background

2.1 Partially Observable Markov Decision Processes (POMDPs)

A partially observable Markov decision process (POMDP) [Åström, 1965] is formalized as a tuple $\langle S, A, T, R, \Omega, O, \gamma \rangle$: states S, actions A, transition function T(s'|s,a) (probability of transitioning to s' from state s via action a), reward function R(s,a), observations Ω , observation function O(o|s',a) (probability of observing o after reaching s' via action a), and discount factor $\gamma \in [0,1)$. Unlike MDPs, agents cannot directly observe states, fundamentally increasing problem complexity.

Agents maintain belief states b(s) - probability distributions over possible states. After action a and observation o, beliefs update via Bayes' rule: $b'(s') = \eta \cdot O(o|s',a) \sum_{s \in S} T(s'|s,a)b(s)$, where η normalizes to ensure $\sum_{s' \in S} b'(s') = 1$. This update encapsulates the agent's knowledge given their action-observation history.

2.2 Stein Variational Gradient Descent (SVGD)

SVGD [Liu, 2017] is a deterministic sampling algorithm that iteratively transports particles $\{x_i\}_{i=1}^n$ to approximate a target distribution p(x) by minimizing KL divergence through functional gradient descent. Particles update via $x_i \leftarrow x_i + \epsilon \phi(x_i)$, where ϵ is step size and the optimal velocity field $\phi^*(x) = \frac{1}{n} \sum_{j=1}^n [k(x_j, x) \nabla_{x_j} \log p(x_j) + \nabla_{x_j} k(x_j, x)]$ belongs to a reproducing kernel Hilbert space with kernel k(x, x') [Liu, 2017].

The update balances exploitation $(k(x_j, x)\nabla_{x_j}\log p(x_j))$ driving particles toward high-density regions) and exploration $(\nabla_{x_j}k(x_j, x))$ creating repulsive forces preventing collapse). The RBF kernel $k(x, x') = \exp(-\frac{1}{h}||x - x'||^2)$ with bandwidth h controls inter-particle interactions [Garreau et al., 2017, Liu, 2017], offering theoretical convergence guarantees with computational efficiency.

However, SVGD struggles in high-dimensional POMDPs where correlation structures $C_{ij} = \frac{\Sigma_{ij}}{\sqrt{\Sigma_{ii}\Sigma_{jj}}}$ (with i,j indexing state dimensions) capture statistical dependencies [Chen et al., 2022]. Standard isotropic RBF kernels create uniform repulsive forces [Zhuo et al., 2017], failing to preserve anisotropic belief distributions' correlation patterns. This causes kernel degeneracy in high dimensions [Chen and Ghattas, 2020]—kernel values become nearly constant—preventing particles from aligning along principal correlation directions, degrading belief approximation and POMDP performance.

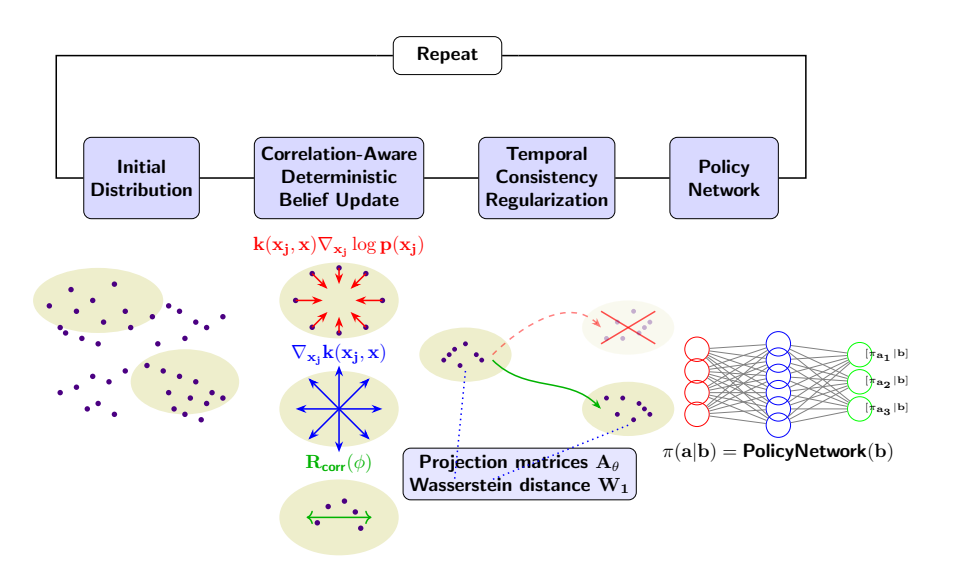
2.3 Projection Methods in Optimal Transport

Optimal Transport (OT) provides a geometric framework for comparing probability distributions via minimal transformation cost [Villani, 2008]. The Wasserstein distance $W_p(\mu,\nu)=\left(\inf_{\gamma\in\Gamma(\mu,\nu)}\int\|x-y\|^pd\gamma(x,y)\right)^{1/p}$ captures both probability mass differences and geometric relationships, where $\Gamma(\mu,\nu)$ denotes joint distributions with marginals μ and ν .

To reduce computational expense in high dimensions, Sliced Wasserstein Distance (SWD) [Rabin et al., 2011] projects distributions onto one-dimensional subspaces: $SW_p(\mu,\nu) = \left(\int_{\mathbb{S}^{d-1}} W_p^p(\mathcal{R}[\mu]_\theta, \mathcal{R}[\nu]_\theta) d\sigma(\theta)\right)^{1/p}$, where $\mathcal{R}[\cdot]_\theta$ denotes the Radon transform along direction θ . Generalized Sliced Wasserstein (GSW) Distance [Kolouri et al., 2019] extends this with nonlinear transformations: $GSW_p(\mu,\nu) = \left(\int_{\Theta} W_p^p(\mathcal{R}_h[\mu]_\theta, \mathcal{R}_h[\nu]_\theta) d\lambda(\theta)\right)^{1/p}$ using parameterized function $h_\theta(x)$, with max-GSW Distance variant: max-GSW $_p(\mu,\nu) = \max_{\theta \in \Theta} W_p(\mathcal{R}_h[\mu]_\theta, \mathcal{R}_h[\nu]_\theta)$.

ESCORT integrates these projection principles as regularization mechanisms within SVGD's update process rather than as distance metrics. This enables learning transformation matrices that identify significant correlation directions while mitigating kernel degeneracy, allowing particles to align along principal correlation directions while maintaining multi-modal diversity—addressing fundamental challenges in complex POMDP belief representation.

3 Approach



• ESCORT Particles — True Distribution Modes — Attractive Forces — Repulsive Forces — Correlation Projections

Figure 1: Overview of the ESCORT framework. The diagram illustrates the iterative process of maintaining accurate belief representations in POMDPs through deterministic particle evolution. Purple dots represent particles, yellow regions show distribution modes, and colored arrows indicate different force types. In the Temporal Consistency component, green arrows represent permissible belief transitions while red crossed arrows indicate prevented unrealistic jumps.

We present ESCORT (Efficient Stein-variational and sliced Consistency-Optimized Representation for Temporal beliefs), a particle-based framework addressing the challenges of belief approximation in complex POMDPs, as illustrated in Figure 1. ESCORT extends SVGD with correlation-aware projections and temporal consistency constraints, enabling effective representation of high-dimensional, multi-modal belief distributions with intricate correlation structures. Through deterministic particle evolution and strategic regularization, our approach maintains particle diversity while preserving dimensional dependencies, overcoming limitations of both parametric methods and traditional particle filters.

3.1 Correlation-Aware Deterministic Belief Update Mechanism

As established in Section 2.2, SVGD addresses particle degeneracy through deterministic evolution that theoretically converges to the target distribution without resampling. SVGD applies the perturbation:

$$\phi^*(x) = \frac{1}{n} \sum_{j=1}^n [k(x_j, x) \nabla_{x_j} \log p(x_j) + \nabla_{x_j} k(x_j, x)]$$
 (1)

In the POMDP context, $p(\cdot)$ represents the belief given by Bayes' rule: $p(s') \propto O(o|s',a) \cdot \sum_s T(s'|s,a)b(s)$, with the score function $\nabla_{x_j} \log p(x_j)$ approximated numerically using finite differences.

This formulation balances attractive forces toward high-density regions with repulsive interactions that maintain particle diversity. However, standard SVGD faces critical limitations in POMDP settings. First, it suffers from kernel degeneracy in high-dimensional state spaces, where the RBF kernel $k(x,x')=\exp(-\frac{1}{h}||x-x'||^2)$ produces nearly uniform values, weakening repulsive forces and leading to mode collapse [Zhuo et al., 2017, Chen and Ghattas, 2020]. More fundamentally, standard SVGD's isotropic RBF kernel creates uniform repulsive forces that fail to preserve the anisotropic correlation patterns inherent in POMDP belief distributions [Wang et al., 2017]. In POMDPs, these correlation structures are captured by the correlation matrix C with elements $C_{ij} = \sum_{ij} / \sqrt{\sum_{ii} \cdot \sum_{jj}}$, where Σ is the covariance matrix. These off-diagonal elements C_{ij} encode critical statistical dependencies between state dimensions—information essential for accurate belief representation and downstream decision quality.

Recent extensions like MP-SVGD [Zhuo et al., 2017] and SVMP [Wang et al., 2018] attempt to address high-dimensional challenges through fixed graphical structures that decompose the kernel into localized interactions. However, these approaches remain insufficient for POMDPs, which require adaptive correlation modeling that dynamically responds to observation-dependent belief changes [Boyen and Koller, 1998]. To address these fundamental limitations, we introduce ESCORT, which implements a complete belief update mechanism that combines deterministic particle evolution with model-based state estimation. The update for each particle is formulated as:

$$x_i^{t+1} = x_i^t + \epsilon \phi_{\text{reg}}^*(x_i^t) + \text{Update}(o_{t+1}, a_t)$$
(2)

where x_i^t represents the *i*-th particle at time step t, ϵ is the step size, ϕ_{reg}^* is our correlation-aware regularized particle evolution function that maintains particle diversity while preserving dimensional dependencies, and Update (o_{t+1}, a_t) incorporates new evidence by shifting particles based on observation likelihoods and transition dynamics. We detail the formulation of both the regularized particle evolution and observation-action update components in the following subsections.

Having established the complete belief update mechanism combining deterministic particle evolution with model-based state estimation, we now detail the correlation-aware regularization term ϕ_{reg}^* that addresses SVGD's limitations in high-dimensional spaces.

3.2 Correlation-Aware Regularization

Drawing inspiration from optimal transport theory, particularly the Generalized Sliced Wasserstein (GSW) distance [Kolouri et al., 2019], we construct our correlation-aware regularization term to address the limitations of standard SVGD discussed before. The key insight from GSW is that projecting high-dimensional distributions onto carefully selected lower-dimensional subspaces can efficiently capture correlation structures while remaining computationally tractable [Kolouri et al., 2019]. By integrating this projection-based approach, ESCORT addresses both critical SVGD limitations: kernel degeneracy is mitigated through dimensionality reduction of distance calculations, while complex correlation structures are preserved by learning projection matrices aligned with dimensional dependencies.

Our correlation-aware regularization term is formulated as:

$$R_{\text{corr}}(\phi) = \mathbb{E}_{x \sim q} \left[\sum_{i=1}^{m} w_i \cdot |A_i^T(\phi(x) - \mathbb{E}_{y \sim q}[\phi(y)])|^2 \right]$$
(3)

where the expectation averages over all particles in the current distribution q, and the summation aggregates contributions from m different projection matrices. Here, ϕ is the particle movement vector

field, $A_i \in \mathbb{R}^{d \times k_i}$ are projection matrices identifying key correlation directions, w_i are importance weights, and $|\cdot|^2$ is squared Euclidean norm. This approach adapts to the anisotropic nature of belief distributions, unlike standard SVGD's isotropic kernel.

The effectiveness of this regularization term depends on identifying projection matrices that capture meaningful correlation structures relative to the target distribution. In the POMDP context, the target distribution p(x) in our SVGD formulation represents the unnormalized posterior belief distribution:

$$p(x) \propto O(o_{t+1}|x, a_t) \cdot \sum_{s \in S} T(x|s, a_t) b_t(s)$$
(4)

where $O(o_{t+1}|x,a_t)$ is the observation likelihood, $\sum_{s\in S} T(x|s,a_t)b_t(s)$ is the predicted belief after transition, and $b_t(s)$ is the previous timestep's belief. This corresponds to the standard POMDP belief update before normalization. Crucially, SVGD directly works with this unnormalized distribution—the normalization constant in the standard Bayes update $b'(s') = \eta \cdot O(o|s',a) \cdot \sum_s T(s'|s,a)b(s)$ is handled implicitly through gradient-based particle evolution, eliminating the computational overhead of explicit normalization while naturally preserving the correlation structures present in the posterior.

To identify and preserve these correlation structures through our regularization term, the projection matrices A_i are initialized using eigenvectors derived from the difference between correlation matrices of the current particle distribution and target distribution: $\Delta C = \operatorname{corr}(X_q) - \operatorname{corr}(X_p)$. The eigenvectors corresponding to the largest eigenvalues of this correlation difference matrix provide initial projection directions that highlight dimensions with significant correlation differences. These initial projections are then optimized to maximize the distance between distributions when projected:

$$A_i^* = \arg \max_{A_i} \mathbb{E}_{(x,y) \sim (q,p)} \left[|A_i^T(x-y)|^2 \right]$$
 (5)

where A_i^* denotes the optimal projection matrix, q represents the current particle distribution, p represents the target distribution, p and p drawn from p, and p drawn from p drawn from p, and p drawn from p

This optimization process ensures that for any belief distribution b(s) with correlation matrix Σ , the regularization term $R_{\rm corr}(\phi)$ with optimized projection matrices A_i preserves the principal correlation directions of Σ under the SVGD update. This theoretical guarantee means that as we increase the number of projection matrices, we can more accurately preserve the correlation structure of complex belief distributions.

Incorporating this correlation-aware regularization into the SVGD framework yields our complete regularized update:

$$\phi_{\text{reg}}^*(x) = \frac{1}{n} \sum_{i=1}^n [k(x_j, x) \nabla_{x_j} \log p(x_j) + \nabla_{x_j} k(x_j, x)] - \lambda \nabla_x R_{\text{corr}}(\phi)$$
 (6)

where λ controls the regularization strength. In our practical implementation, both the projection matrices A_i and their importance weights w_i are updated iteratively alongside the particle positions, ensuring that they adapt to the evolving belief distribution throughout the POMDP planning process.

3.3 Model-Based Belief Update

The Model-Based Belief Update component Update (o_{t+1}, a_t) in our belief update equation integrates new observations and actions into the belief distribution. While ϕ_{reg}^* maintains representational properties, this component leverages the POMDP model's dynamics to shift particles according to actual environment behavior. Unlike DVRL which learns transition and observation models [Igl et al., 2018], ESCORT assumes known POMDP models with state transition function T(s'|s,a) and observation function O(o|s',a). This model-based design is essential for two reasons: first, accurate likelihood gradients from known dynamics enable SVGD's deterministic evolution, correlation-aware regularization, and temporal consistency to function correctly through precise displacement vectors that specify how each particle should move; second, it enables fair comparison

with existing particle-based methods by isolating our belief representation innovations from model learning errors.

Given a particle set $\{x_i^t\}_{i=1}^n$ representing the belief at time t, an action a_t , and observation o_{t+1} , the model-based update proceeds in three steps. First, each particle is propagated through the transition model: $\tilde{x}_i^{t+1} = T(x_i^t, a_t) + \eta_i$ where $\eta_i \sim \mathcal{N}(0, \Sigma_{\text{trans}})$ represents transition noise. Next, the observation likelihood $w_i = O(o_{t+1}|\tilde{x}_i^{t+1}, a_t)$ is computed for each predicted particle, quantifying how well it explains the received observation. The final update combines these components as Update $(o_{t+1}, a_t) = (\tilde{x}_i^{t+1} - x_i^t) + \Delta x_i(w_i)$, where the first term represents the state change due to the transition model and the displacement term $\Delta x_i(w_i) = \alpha \cdot w_i \cdot (\mu_{obs} - \tilde{x}_i)$ provides likelihood-weighted adjustment. Here, $\mu_{obs} = (\sum_j w_j \tilde{x}_j)/(\sum_j w_j)$ is the observation-weighted mean and $\alpha \in (0,1)$ controls correction strength. Unlike the standard Bayes filter's analytical update $b'(s') = \eta \cdot O(o|s', a) \cdot \sum_s T(s'|s, a)b(s)$, this particle-based formulation provides a Monte Carlo approximation without requiring analytical tractability. By incorporating observation information through local adjustments that pull particles toward high-likelihood regions rather than global resampling, this deterministic approach avoids particle degeneracy while maintaining multi-modal coverage and preserving the correlation structures that stochastic resampling destroys.

3.4 Temporal Consistency Regularization

While the correlation-aware regularization term focuses on preserving dimensional dependencies within individual belief states, ESCORT introduces an additional temporal dimension requiring consistency across consecutive belief updates. In POMDPs, beliefs can change dramatically between timesteps, especially when observations are noisy or ambiguous, leading to abrupt and potentially unrealistic belief jumps that compromise decision quality [Li et al., 2014]. These sudden belief jumps not only lead to erratic policy behavior but also destroy previously learned correlation structures between state variables, causing the belief representation to lose critical dimensional dependencies that were carefully preserved by the correlation-aware regularization mechanism.

To address this critical challenge, we introduce a temporal consistency regularization mechanism that complements our correlation-aware regularized particle evolution. This mechanism ensures that belief updates respect the underlying temporal dynamics of the environment while still incorporating new evidence from observations. Mathematically, we define temporal consistency as the expected transport cost between consecutive belief distributions when projected onto informative subspaces. The temporal consistency constraint is formulated as:

$$L_{\text{temp}} = \int_{\Theta} W_1((A_{\theta})^{\top} b_{t+1}, (A_{\theta})^{\top} b_t) d\lambda(\theta)$$
 (7)

where b_{t+1} represents the current belief after applying all updates (transition model, observation update, and SVGD), b_t represents the previous timestep's belief, W_1 is the 1-Wasserstein distance measuring minimum transport cost between beliefs, and $A_\theta \in \mathbb{R}^{d \times k}$ are learned projection matrices identifying subspaces where temporal changes are most informative.

Here, $\lambda(\theta)$ is a probability distribution over the projection parameter space Θ . Together with the projection matrices A_{θ} , this mechanism identifies temporal patterns between timesteps— A_{θ} provides the projection directions while $\lambda(\theta)$ assigns importance weights to each direction, quantifying which dimensions should evolve smoothly (high weight on projections revealing problematic jumps) versus which can change rapidly (low weight on naturally variable dimensions). This direction-specific regularization constrains belief updates heavily along projections that reveal unrealistic jumps while allowing natural evolution where temporal variation is expected. In contrast, the A_i matrices in our correlation-aware regularization (Section 3.2) serve a fundamentally different purpose: they preserve spatial correlations within each timestep, capturing how dimensions relate to each other at a single moment rather than across time.

In practice, this integral is approximated as a weighted sum over a finite set of optimized projection directions, with weights representing their relative importance. By regularizing the distance between consecutive belief states, we prevent unrealistically large belief jumps while still allowing the belief to adapt to new information. Detailed implementation is provided in Appendix.

3.5 Particle-Based Policy Network

After establishing our particle-based belief representation that accurately captures complex uncertainty structures, we leverage these beliefs directly for decision-making through a specialized policy network architecture—the only learned component in ESCORT. The network processes particles through two key stages: a per-particle encoder f_{particle} independently processes each particle x_i into feature representations $h_i = f_{\text{particle}}(x_i)$ using a multi-layer neural network, then these features are aggregated using a permutation-invariant operation (mean pooling) followed by further processing: $b_{\text{encoded}} = f_{\text{belief}}(\frac{1}{n}\sum_{i=1}^n h_i)$. This two-stage approach accounts for both individual particle states and their collective distribution properties, enabling effective reasoning about multi-modal uncertainties.

The policy is optimized using policy gradient methods. Given experience tuples (b_t, a_t, r_t, b_{t+1}) , the objective function is $\mathcal{L}(\theta) = -\mathbb{E}_{(b_t, a_t, r_t)}[\log \pi_{\theta}(a_t|b_t) \cdot R_t]$, where R_t is the discounted return. For continuous actions, entropy regularization is applied: $\mathcal{L}(\theta) = -\mathbb{E}[\log \pi_{\theta}(a_t|b_t) \cdot R_t + \alpha \mathcal{H}(\pi_{\theta}(\cdot|b_t))]$. This approach directly optimizes the policy to maximize expected returns based on the particle representation of beliefs.

For action selection, ESCORT supports both discrete and continuous spaces. With discrete actions, the network outputs a probability distribution $\pi(a|b) = \operatorname{softmax}(g_{\operatorname{action}}(b_{\operatorname{encoded}}))$. For continuous actions, it parameterizes a Gaussian distribution with $(\mu(b), \log \sigma(b)) = (g_{\operatorname{mean}}(b_{\operatorname{encoded}}), g_{\operatorname{std}}(b_{\operatorname{encoded}}))$. Actions can be selected either deterministically (most probable action or mean) or stochastically (sampling from the output distribution).

4 Experiments

We designed our experiments to evaluate ESCORT's effectiveness in two key aspects: (1) maintaining accurate belief representations in challenging POMDP domains and (2) approximating complex, multi-modal distributions with correlated state variables across various dimensionalities. This comprehensive evaluation aims to validate ESCORT's ability to address the complex belief distribution we identified earlier.

Baselines: We compare against state-of-the-art methods from different POMDP belief approximation categories: *Particle-based methods* including *SIR* (Sequential Importance Resampling) and *POMCPOW* [Sunberg and Kochenderfer, 2018] that use stochastic resampling, leading to particle degeneracy and mode collapse in high-dimensional correlated spaces; *Parametric belief representations* like *DVRL* [Igl et al., 2018] that encode beliefs into fixed-dimensional VAE representations, sacrificing expressiveness for multi-modal distributions; and *Deterministic sampling* via *SVGD* [Liu, 2017] offering gradient-based particle evolution but suffering from kernel degeneracy without correlation preservation. Additional comparative methods are discussed in the Appendix.

Evaluation Metrics: We assess ESCORT using two metric groups: POMDP-specific metrics measuring policy performance and distribution approximation metrics evaluating belief representation quality. For POMDP tasks, we report Average Return (position error, lower is better) reflecting navigation/localization accuracy across environments. For distribution approximation, we track Maximum Mean Discrepancy and Sliced Wasserstein Distance (statistical similarity between distributions), Mode Coverage Ratio (proportion of maintained hypotheses), and Correlation Error (accuracy of captured dimensional relationships). Detailed metric specifications, computation methods, and interpretations are provided in the Appendix.

Experimental Setup: We evaluate ESCORT against baselines across three POMDP domains: Light-Dark Navigation, Kidnapped Robot, and Multi-Target Tracking. We additionally test on synthetic multi-modal distributions (1D-20D). All methods use consistent configurations: 1000 particles, step size ε =0.01 with adaptive decay, kernel bandwidth via median heuristic. DVRL uses latent dimensions matching state space; SIR/POMCPOW receive equivalent computational budgets. Experiments span 30 independent runs on Intel i9-13900K CPU. Our computational analysis (Appendix D) shows ESCORT scales as $O(d^{1.67})$ with correlation-aware term dominating at high dimensions, yielding 40% correlation error improvement. Full specifications in Appendix.

Table 1: Performance comparison across POMDP environments including ablation study. Values represent average position error (with standard error) after task completion—lower values indicate better performance. ESCORT variants demonstrate the contribution of each component to the overall framework effectiveness, while the full ESCORT method consistently outperforms all baselines across environments, with increasing advantages as dimensionality grows. Detailed environment specifications, experimental protocols, and additional analyses are provided in the Appendix.

Method	Light-Dark (10D)	Kidnapped Robot (20D)	Target Tracking (20D)
ESCORT Vai	riants		
Full	0.347 ± 0.03	$\textbf{9.063} \pm \textbf{0.51}$	$\textbf{3.665} \pm \textbf{0.31}$
NoCorr	0.381 ± 0.07	10.246 ± 0.35	4.213 ± 0.59
NoTemp	$\textbf{0.321} \pm \textbf{0.03}$	10.859 ± 0.51	3.874 ± 0.43
NoProj	0.359 ± 0.09	9.654 ± 0.32	3.90 ± 0.42
Baselines			
SVGD	0.379 ± 0.03	10.906 ± 0.49	4.295 ± 0.22
DVRL	1.557 ± 0.10	14.309 ± 0.60	4.33 ± 0.09
POMCPOW	2.12 ± 0.24	12.023 ± 0.55	4.611 ± 0.09

4.1 Domains

Light-Dark Navigation: Our 10D implementation (5D position, 5D velocity) extends the traditional POMDP testbed [Platt et al., 2010, Silver and Veness, 2010] with varying observation quality tied to spatial "light level"—precise in well-lit areas but noisy in dark regions. This environment tests belief tracking under nonuniform observation noise, generating distributions ranging from precise unimodal to complex multimodal patterns with inherent correlations. Performance is measured by Euclidean distance to goal (lower is better), reflecting how accurately the agent navigates despite uncertain observations.

Kidnapped Robot Problem: This classical robotics challenge [Choset et al., 2005] is scaled to 20 dimensions (position, orientation, steering, sensor calibration, and feature descriptors). A robot must localize within a map containing perceptually similar landmark patterns, creating multi-modal beliefs due to ambiguous observations. Performance is evaluated by position error after fixed time steps, quantifying localization accuracy despite ambiguous landmarks.

Multiple Target Tracking: Our 20D tracking environment [Rong Li and Jilkov, 2003] challenges an agent (4D) to track four targets (16D) under visibility zones with varying noise, occlusion regions, and identity confusion areas. This domain tests simultaneous handling of high dimensionality, multi-modality, and correlation preservation. Performance is measured by the mean position error across all targets, indicating tracking accuracy despite occlusions and identity ambiguities. Detailed specifications for all environments are provided in the Appendix.

4.2 Results

Table 1 demonstrates ESCORT's superior performance across POMDP domains of varying dimensionality. In the 10D Light-Dark environment, ESCORT achieves 8.5% improvement over SVGD and 83.6% over POMCPOW, with advantages increasing in the 20D domains—achieving 16.9% and 24.7% improvements over SVGD in Kidnapped Robot and Target Tracking respectively. This confirms that ESCORT's advantages become more pronounced as dimensionality grows. The ablation study reveals how each component contributes to ESCORT's success. Correlation-aware regularization emerges as the most critical component, with ESCORT-NoCorr showing 9.8-15% performance degradation that scales with dimensionality, confirming its importance in preserving belief structure. Temporal consistency exhibits domain-dependent effects: while ESCORT-NoTemp surprisingly outperforms the full method in Light-Dark (0.321 vs 0.347)—suggesting symmetric patterns may benefit from unrestricted mode transitions—it proves essential in complex 20D environments with 19.8% degradation in Kidnapped Robot where maintaining hypothesis continuity is crucial. Projection matrices (ESCORT-NoProj) provide consistent moderate benefits that scale from 3.5% in Light-Dark to 6.5% in Kidnapped Robot, demonstrating their role in efficient correlation capture.

Table 2 reveals ESCORT's specific advantages in maintaining accurate belief distributions. While SVGD performs comparably in lower dimensions, where projection regularization offers limited

Table 2: Comparison of belief approximation methods across different dimensional spaces. MMD and Wasserstein/Sliced Wasserstein measure distribution similarity (lower is better); Correlation Error quantifies dimensional dependency accuracy (lower is better); Mode Coverage indicates successful mode representation (higher is better). Results show mean ± standard error across multiple random initializations. Correlation error is not applicable for 1D. Detailed environment specifications, distribution characteristics, and metric calculations are provided in the Appendix.

Metric	ESCORT	SVGD	DVRL	SIR
	1D Experiment			
Maximum Mean Discrepancy	0.057 ± 0.01	$\textbf{0.012} \pm \textbf{0.01}$	0.216 ± 0.05	0.116 ± 0.07
Wasserstein	0.549 ± 0.04	$\textbf{0.305} \pm \textbf{0.02}$	1.967 ± 0.07	0.811 ± 0.22
Mode Coverage Ratio	$\textbf{1.0} \pm \textbf{0.0}$	$\textbf{1.0} \pm \textbf{0.0}$	0.867 ± 0.13	$\textbf{1.0} \pm \textbf{0.0}$
	2D Experiment			
Maximum Mean Discrepancy	$\textbf{0.052} \pm \textbf{0.02}$	0.062 ± 0.01	0.071 ± 0.01	0.2288 ± 0.04
Sliced Wasserstein	$\textbf{0.263} \pm \textbf{0.01}$	0.383 ± 0.01	0.749 ± 0.14	1.397 ± 0.11
Correlation Error	$\textbf{0.491} \pm \textbf{0.16}$	0.5178 ± 0.04	0.6594 ± 0.09	0.8285 ± 0.28
Mode Coverage	$\textbf{1.0} \pm \textbf{0.0}$	$\textbf{1.0} \pm \textbf{0.0}$	$\textbf{1.0} \pm \textbf{0.0}$	$\textbf{1.0} \pm \textbf{0.0}$
	3D Experiment			
Maximum Mean Discrepancy	0.002 ± 0.002	0.008 ± 0.009	0.361 ± 0.01	0.414 ± 0.06
Sliced Wasserstein	$\textbf{0.305} \pm \textbf{0.01}$	0.481 ± 0.02	1.442 ± 0.04	2.656 ± 0.34
Correlation Error	$\textbf{0.761} \pm \textbf{0.004}$	0.819 ± 0.02	0.882 ± 0.01	1.003 ± 0.01
Mode Coverage	$\textbf{1.0} \pm \textbf{0.0}$	$\textbf{1.0} \pm \textbf{0.0}$	$\textbf{1.0} \pm \textbf{0.0}$	$\textbf{1.0} \pm \textbf{0.0}$
	5D Experiment			
Maximum Mean Discrepancy	0.05 ± 0.003	0.09 ± 0.07	0.263 ± 0.004	0.394 ± 0.009
Sliced Wasserstein	$\textbf{0.301} \pm \textbf{0.01}$	0.3987 ± 0.02	1.0838 ± 0.01	2.939 ± 0.26
Correlation Error	$\textbf{0.7224} \pm \textbf{0.006}$	0.7401 ± 0.014	0.823 ± 0.011	0.997 ± 0.003
Mode Coverage	$\textbf{1.0} \pm \textbf{0.0}$	$\textbf{1.0} \pm \textbf{0.0}$	$\textbf{1.0} \pm \textbf{0.0}$	0.125 ± 0.0
20D Experiment				
Maximum Mean Discrepancy	0.005 ± 0.0008	0.006 ± 0.0006	0.264 ± 0.005	0.584 ± 0.008
Sliced Wasserstein	$\textbf{0.326} \pm \textbf{0.007}$	0.393 ± 0.005	1.117 ± 0.025	2.854 ± 0.187
Correlation Error	$\textbf{0.556} \pm \textbf{0.03}$	0.589 ± 0.05	0.708 ± 0.03	0.640 ± 0.01
Mode Coverage	$\textbf{1.0} \pm \textbf{0.0}$	$\textbf{1.0} \pm \textbf{0.0}$	0.58 ± 0.04	0.12 ± 0.04

benefits and kernel degeneracy is less severe, ESCORT consistently outperforms all methods at higher dimensionality, with up to 37.5% lower correlation error than traditional particle filters. Most striking is mode coverage in high dimensions—ESCORT maintains perfect coverage in 20D spaces where SIR experiences catastrophic mode collapse (0.12 coverage) and DVRL significant degradation (0.58 coverage). This validates our approach's ability to preserve dimensional dependencies while preventing particle degeneracy across all relevant modes. A comprehensive interpretation of these results, including detailed ablation studies and statistical significance analyses, is provided in the Appendix.

5 Conclusion

We presented ESCORT, a particle-based framework extending SVGD with correlation-aware projections and temporal consistency constraints to address the challenge of representing complex beliefs in high-dimensional POMDPs. Our approach overcomes key limitations in existing methods by mitigating kernel degeneracy, maintaining expressiveness without parametric compression, and preventing particle collapse through deterministic evolution. Evaluations across POMDP domains and synthetic distributions demonstrate significant improvements in both belief accuracy and decision quality.

Despite these advances, ESCORT faces practical limitations. The computational overhead of correlation matrix computation and projection optimization increases with dimensionality, potentially limiting real-time deployment. More fundamentally, our reliance on known transition and observation models restricts applicability to domains where accurate models are unavailable. Future work will address these limitations through GPU-accelerated implementations for real-time performance, adaptive projection techniques that reduce computational burden, and integration with model learning approaches to enable deployment in unknown environments.

6 Acknowledgements

This material is based upon work supported by the National Science Foundation (NSF) under Grant CNS-2238815 and by the Defense Advanced Research Projects Agency (DARPA) and US Air Force Research Lab (AFRL) under the Assured Neuro Symbolic Learning and Reasoning program. Results presented in this paper were obtained using the Chameleon testbed supported by the National Science Foundation. Any opinions, findings, conclusions, or recommendations expressed in this material are those of the authors and do not necessarily reflect the views of the NSF, DARPA, or AFRL.

References

- Marc G. Bellemare, Yavar Naddaf, Joel Veness, and Michael Bowling. The arcade learning environment: an evaluation platform for general agents. *J. Artif. Int. Res.*, 47(1):253–279, May 2013. ISSN 1076-9757.
- Xavier Boyen and Daphne Koller. Tractable inference for complex stochastic processes. *ArXiv*, abs/1301.7362, 1998. URL https://api.semanticscholar.org/CorpusID:5556701.
- Alex Brooks, Alexei Makarenko, Stefan Williams, and Hugh Durrant-Whyte. Parametric pomdps for planning in continuous state spaces. *Robotics and Autonomous Systems*, 54(11):887–897, 2006. ISSN 0921-8890. doi: https://doi.org/10.1016/j.robot.2006.05.007. URL https://www.sciencedirect.com/science/article/pii/S0921889006000960. Planning Under Uncertainty in Robotics.
- Peng Chen and Omar Ghattas. Projected stein variational gradient descent. In *Proceedings of the 34th International Conference on Neural Information Processing Systems*, NIPS '20, Red Hook, NY, USA, 2020. Curran Associates Inc. ISBN 9781713829546.
- Xiaoyu Chen, Yao Mu, Ping Luo, Sheng Li, and Jianyu Chen. Flow-based recurrent belief state learning for pomdps. In *International Conference on Machine Learning*, 2022. URL https://api.semanticscholar.org/CorpusID:248986064.
- Howie Choset, Kevin M. Lynch, Seth Hutchinson, George Kantor, Wolfram Burgard, Lydia E. Kavraki, and Sebastian Thrun. *Principles of Robot Motion: Theory, Algorithms, and Implementation*, chapter 13, pages 249–253. MIT Press, Cambridge, MA, 2005.
- Damien Garreau, Wittawat Jitkrittum, and Motonobu Kanagawa. Large sample analysis of the median heuristic. *arXiv: Statistics Theory*, 2017. URL https://api.semanticscholar.org/CorpusID:88514908.
- Neil J. Gordon, David Salmond, and Adrian F. M. Smith. Novel approach to nonlinear/non-gaussian bayesian state estimation. In *IEE Proceedings F Radar and Signal Processing*, 1993.
- Charles R. Harris, K. Jarrod Millman, Stéfan J. van der Walt, Ralf Gommers, Pauli Virtanen, David Cournapeau, Eric Wieser, Julian Taylor, Sebastian Berg, Nathaniel J. Smith, Robert Kern, Matti Picus, Stephan Hoyer, Marten H. van Kerkwijk, Matthew Brett, Allan Haldane, Jaime Fernández del Río, Mark Wiebe, Pearu Peterson, Pierre Gérard-Marchant, Kevin Sheppard, Tyler Reddy, Warren Weckesser, Hameer Abbasi, Christoph Gohlke, and Travis E. Oliphant. Array programming with numpy. *Nature*, 585(7825):357–362, September 2020. ISSN 1476-4687. doi: 10.1038/s41586-020-2649-2. URL http://dx.doi.org/10.1038/s41586-020-2649-2.
- Matthew J. Hausknecht and Peter Stone. Deep recurrent q-learning for partially observable mdps. *ArXiv*, abs/1507.06527, 2015. URL https://api.semanticscholar.org/CorpusID: 8696662.
- Maximilian Igl, Luisa Zintgraf, Tuan Anh Le, Frank Wood, and Shimon Whiteson. Deep variational reinforcement learning for POMDPs. In Jennifer Dy and Andreas Krause, editors, *Proceedings of the 35th International Conference on Machine Learning*, volume 80 of *Proceedings of Machine Learning Research*, pages 2117–2126. PMLR, 10–15 Jul 2018. URL https://proceedings.mlr.press/v80/igl18a.html.

- Leslie Pack Kaelbling, Michael L. Littman, and Anthony R. Cassandra. Planning and acting in partially observable stochastic domains. *Artificial Intelligence*, 101(1):99–134, 1998. ISSN 0004-3702. doi: https://doi.org/10.1016/S0004-3702(98)00023-X. URL https://www.sciencedirect.com/science/article/pii/S000437029800023X.
- Diederik P. Kingma and Max Welling. Auto-encoding variational bayes. *CoRR*, abs/1312.6114, 2013. URL https://api.semanticscholar.org/CorpusID:216078090.
- Soheil Kolouri, Kimia Nadjahi, Umut Simsekli, Roland Badeau, and Gustavo Rohde. Generalized sliced wasserstein distances. In H. Wallach, H. Larochelle, A. Beygelzimer, F. d'Alché-Buc, E. Fox, and R. Garnett, editors, Advances in Neural Information Processing Systems, volume 32. Curran Associates, Inc., 2019.
- Solomon Kullback and R. A. Leibler. On information and sufficiency. *Annals of Mathematical Statistics*, 22:79–86, 1951. URL https://api.semanticscholar.org/CorpusID: 120349231.
- Hanna Kurniawati. Partially observable markov decision processes and robotics. *Annual Review of Control, Robotics, and Autonomous Systems*, 5:253–277, 2022. ISSN 2573-5144. doi: 10.1146/annurev-control-042920-092451. Publisher Copyright: Copyright © 2022 by Annual Reviews.
- Siu Kwan Lam, Antoine Pitrou, and Stanley Seibert. Numba: a llvm-based python jit compiler. In *Proceedings of the Second Workshop on the LLVM Compiler Infrastructure in HPC*, LLVM '15, New York, NY, USA, 2015. Association for Computing Machinery. ISBN 9781450340052. doi: 10.1145/2833157.2833162. URL https://doi.org/10.1145/2833157.2833162.
- Mikko Lauri, David Hsu, and Joni Pajarinen. Partially observable markov decision processes in robotics: A survey. *IEEE Transactions on Robotics*, 39(1):21–40, 2023. doi: 10.1109/TRO.2022. 3200138.
- Tiancheng Li, Shudong Sun, Tariq Pervez Sattar, and Juan Manuel Corchado. Fight sample degeneracy and impoverishment in particle filters: A review of intelligent approaches. *Expert Systems with Applications*, 41(8):3944–3954, 2014. ISSN 0957-4174. doi: https://doi.org/10.1016/j.eswa.2013.12.031. URL https://www.sciencedirect.com/science/article/pii/S0957417413010063.
- Qiang Liu. Stein variational gradient descent as gradient flow. In I. Guyon, U. Von Luxburg, S. Bengio, H. Wallach, R. Fergus, S. Vishwanathan, and R. Garnett, editors, *Advances in Neural Information Processing Systems*, volume 30. Curran Associates, Inc., 2017.
- Xiao Ma, Peter Karkus, David Hsu, Wee Sun Lee, and Nan Ye. Discriminative particle filter reinforcement learning for complex partial observations. *ArXiv*, abs/2002.09884, 2020. URL https://api.semanticscholar.org/CorpusID:211259464.
- Marlos C. Machado, Marc G. Bellemare, Erik Talvitie, Joel Veness, Matthew Hausknecht, and Michael Bowling. Revisiting the arcade learning environment: evaluation protocols and open problems for general agents. *J. Artif. Int. Res.*, 61(1):523–562, January 2018. ISSN 1076-9757.
- Robert Platt, Russ Tedrake, Leslie Pack Kaelbling, and Tomas Lozano-Perez. Belief space planning assuming maximum likelihood observations. In *Robotics: Science and Systems*, 2010. URL https://api.semanticscholar.org/CorpusID:2693863.
- Martin L. Puterman. *Markov Decision Processes: Discrete Stochastic Dynamic Programming*. John Wiley & Sons, 1994.
- J. Rabin, G. Peyre, J. Delon, and M. Bernot. Wasserstein barycenter and its application to texture mixing. Scale Space and Variational Methods in Computer Vision, 2011. pp. 435-446.
- X. Rong Li and V.P. Jilkov. Survey of maneuvering target tracking. part i. dynamic models. *IEEE Transactions on Aerospace and Electronic Systems*, 39(4):1333–1364, 2003. doi: 10.1109/TAES. 2003.1261132.

- Nicholas Roy and Geoffrey J Gordon. Exponential family pca for belief compression in pomdps. In S. Becker, S. Thrun, and K. Obermayer, editors, *Advances in Neural Information Processing Systems*, volume 15. MIT Press, 2002.
- David Silver and Joel Veness. Monte-carlo planning in large pomdps. In J. Lafferty, C. Williams, J. Shawe-Taylor, R. Zemel, and A. Culotta, editors, *Advances in Neural Information Processing Systems*, volume 23. Curran Associates, Inc., 2010.
- Adhiraj Somani, Nan Ye, David Hsu, and Wee Sun Lee. Despot: Online pomdp planning with regularization. In C.J. Burges, L. Bottou, M. Welling, Z. Ghahramani, and K.Q. Weinberger, editors, *Advances in Neural Information Processing Systems*, volume 26. Curran Associates, Inc., 2013.
- Zachary Sunberg and Mykel Kochenderfer. Online algorithms for pomdps with continuous state, action, and observation spaces, 2018. URL https://arxiv.org/abs/1709.06196.
- Sebastian Thrun, Wolfram Burgard, and Dieter Fox. Probabilistic Robotics. MIT Press, Cambridge, MA, 2005. ISBN 0-262-20162-3.
- Mark Towers, Ariel Kwiatkowski, Jordan Terry, John U. Balis, Gianluca De Cola, Tristan Deleu, Manuel Goulão, Andreas Kallinteris, Markus Krimmel, Arjun KG, Rodrigo Perez-Vicente, Andrea Pierré, Sander Schulhoff, Jun Jet Tai, Hannah Tan, and Omar G. Younis. Gymnasium: A standard interface for reinforcement learning environments, 2024. URL https://arxiv.org/abs/2407.17032.
- Cédric Villani. *Optimal transport Old and new*, volume 338, pages xxii+973. Springer-Verlag, 01 2008. doi: 10.1007/978-3-540-71050-9.
- Dilin Wang, Zhe Zeng, and Qiang Liu. Structured stein variational inference for continuous graphical models. *ArXiv*, abs/1711.07168, 2017. URL https://api.semanticscholar.org/CorpusID:28924187.
- Dilin Wang, Zhe Zeng, and Qiang Liu. Stein variational message passing for continuous graphical models. In Jennifer Dy and Andreas Krause, editors, *Proceedings of the 35th International Conference on Machine Learning*, volume 80 of *Proceedings of Machine Learning Research*, pages 5219–5227. PMLR, 10–15 Jul 2018. URL https://proceedings.mlr.press/v80/wang181.html.
- Wei Wei, Lijun Zhang, Lin Li, Huizhong Song, and Jiye Liang. Set-membership belief state-based reinforcement learning for POMDPs. In Andreas Krause, Emma Brunskill, Kyunghyun Cho, Barbara Engelhardt, Sivan Sabato, and Jonathan Scarlett, editors, *Proceedings of the 40th International Conference on Machine Learning*, volume 202 of *Proceedings of Machine Learning Research*, pages 36856–36867. PMLR, 23–29 Jul 2023.
- Chenyang Wu, Guoyu Yang, Zongzhang Zhang, Yang Yu, Dong Li, Wulong Liu, and Jianye Hao. Adaptive online packing-guided search for pomdps. In M. Ranzato, A. Beygelzimer, Y. Dauphin, P.S. Liang, and J. Wortman Vaughan, editors, *Advances in Neural Information Processing Systems*, volume 34, pages 28419–28430. Curran Associates, Inc., 2021.
- Chiyuan Zhang, Samy Bengio, Moritz Hardt, Benjamin Recht, and Oriol Vinyals. Understanding deep learning requires rethinking generalization. *ArXiv*, abs/1611.03530, 2016. URL https://api.semanticscholar.org/CorpusID:6212000.
- Yunuo Zhang, Baiting Luo, Ayan Mukhopadhyay, Daniel Stojcsics, Daniel Elenius, Anirban Roy, Susmit Jha, Miklos Maroti, Xenofon Koutsoukos, Gabor Karsai, and Abhishek Dubey. Shrinking pomcp: A framework for real-time uav search and rescue. In 2024 International Conference on Assured Autonomy (ICAA), pages 48–57, 2024. doi: 10.1109/ICAA64256.2024.00016.
- Yunuo Zhang, Baiting Luo, Ayan Mukhopadhyay, and Abhishek Dubey. Observation adaptation via annealed importance resampling for partially observable markov decision processes. *Proceedings of the International Conference on Automated Planning and Scheduling*, 35(1):306–314, Sep. 2025. doi: 10.1609/icaps.v35i1.36132. URL https://ojs.aaai.org/index.php/ICAPS/article/view/36132.

- Pengfei Zhu, Xin Li, Pascal Poupart, and Guanghui Miao. On improving deep reinforcement learning for pomdps, 2018. URL https://arxiv.org/abs/1704.07978.
- Jingwei Zhuo, Chang Liu, Jiaxin Shi, Jun Zhu, Ning Chen, and Bo Zhang. Message passing stein variational gradient descent. In *International Conference on Machine Learning*, 2017. URL https://api.semanticscholar.org/CorpusID:51877948.
- K.J Åström. Optimal control of markov processes with incomplete state information. *Journal of Mathematical Analysis and Applications*, 10(1):174–205, 1965. ISSN 0022-247X. doi: https://doi.org/10.1016/0022-247X(65)90154-X. URL https://www.sciencedirect.com/science/article/pii/0022247X6590154X.

Algorithm 1: ESCORT

```
Input:
                                                                                                                              x_i^+ \leftarrow x_i with j-th dimension += \epsilon_j
                                                                                                     41:
                                                                                                                             n: number of particles
                                                                                                     42:
      d: state dimensionality
                                                                                                      43:
      h: kernel bandwidth
                                                                                                      44:
                                                                                                                             scores[i, j] \leftarrow \frac{\log(p_i^+) - \log(p_i^-)}{2\epsilon_i}
      \epsilon: step size for updates
                                                                                                      45:
      \lambda_{\rm c}: correlation regularization weight
                                                                                                                        end for
                                                                                                      46:
      \lambda_{\rm t}: temporal consistency weight
                                                                                                      47:
                                                                                                                  end for
      m: number of projection matrices
                                                                                                                  return clip(scores, -100, 100), log_probs
                                                                                                      48:
      T: transition model
                                                                                                           end function
                                                                                                      49:
      O: observation model
                                                                                                     50:
 1: Initialize particles \{x_i^0\}_{i=1}^n \sim \text{initial belief}
                                                                                                           function OptProj(\{x_i\}_{i=1}^n, \{x_i^{\text{prev}}\}_{i=1}^n)
                                                                                                     51:
 2: Initialize projection matrices \{A_j\}_{j=1}^m with random
                                                                                                                  \Sigma \leftarrow \text{Covariance}(\{x_i\}_{i=1}^n)
                                                                                                      52:
      orthonormal matrices
                                                                                                                  \Sigma_{\text{prev}} \leftarrow \text{Covariance}(\{x_i^{\text{prev}}\}_{i=1}^n)
                                                                                                     53:
 3: Initialize projections \mathcal{A} = \{(A_j, w_j)\}_{j=1}^m, A_j \in \mathbb{R}^{d \times d}
                                                                                                                  \Delta C \leftarrow \operatorname{Correlation}(\Sigma) - \operatorname{Correlation}(\Sigma_{\operatorname{prev}})
                                                                                                      54:
      orthonormal, w_j = \frac{1}{m}
                                                                                                                  Extract eigenvectors \{v_k\}_{k=1}^d and eigenvalues
                                                                                                      55:
 4: t \leftarrow 0
                                                                                                                  \{\lambda_k\}_{k=1}^d \text{ of } \Delta C
                                                                                                      56:
 5: while not terminated do
                                                                                                                  Initialize \{A_j\}_{j=1}^m with top eigenvectors
                                                                                                      57:
            a_t \leftarrow \text{SELECTACTION}(\{x_i^t\}_{i=1}^n, \text{policy})
 6:
                                                                                                                  or random orthogonal vectors
                                                                                                      58:
            Execute a_t, receive observation o_{t+1}
 7:
                                                                                                      59:
                                                                                                                  for iteration = 1 to optimization_steps do
           Execute u_t, receive observation v_{t+1}
\{x_i^{\text{prev}}\}_{i=1}^n \leftarrow \{x_i^t\}_{i=1}^n
\eta_i \sim \mathcal{N}(0, \Sigma_{\text{trans}})
\{\tilde{x}_i^{t+1}\}_{i=1}^n \leftarrow \{T(x_i^t, a_t) + \eta_i\}_{i=1}^n
\text{score} \leftarrow \text{ComputeScore}(\{\tilde{x}_i^{t+1}\}_{i=1}^n, o_{t+1}, O)
 8:
                                                                                                                        Compute projected distributions for each
                                                                                                      60:
 9:
                                                                                                                        direction
                                                                                                      61:
10:
                                                                                                                        Update \{A_j\}_{j=1}^m to maximize Wasserstein
                                                                                                      62:
11:
                                                                                                      63:
                                                                                                                        distance between projections
            \{A_j, w_j\}_{j=1}^m \leftarrow \text{OptProj}(\{\tilde{x}_i^{t+1}\}_{i=1}^{n-1}, \{x_i^{\text{prev}}\}_{i=1}^n)
12:
                                                                                                                        Orthonormalize \{A_j\}_{j=1}^m
Update weights \{w_j\}_{j=1}^m based on contribution
                                                                                                      64:
            X^{t+1} \leftarrow \text{RegSVGD}(\tilde{X}^{t+1}, \text{score}, \mathcal{A}, \lambda_c)
13:
                                                                                                     65:
            if t > 0 and \lambda_t > 0 then
14:
                                                                                                     66:
                                                                                                                        to distance
                  X^{t+1} \leftarrow \text{TempCons}(X^{t+1}, X^{\text{prev}}, \mathcal{A}, \lambda_t)
15:
                                                                                                      67:
                                                                                                                 \begin{array}{l} \{w_j\}_{j=1}^m \leftarrow \{w_j/\sum_{k=1}^m w_k\}_{j=1}^m \\ \mathbf{return} \ \{A_j\}_{j=1}^m, \{w_j\}_{j=1}^m \end{array}
            end if
16:
                                                                                                      68:
            t \leftarrow t + 1
17:
                                                                                                      69:
18: end while
                                                                                                      70: end function
19:
                                                                                                     71:
     function Selectaction(\{x_i\}_{i=1}^n, policy)
                                                                                                      72: function TEMPCONS(X^{t+1}, X^{\text{prev}}, \{A_j\}_{j=1}^m, \lambda_t)
            \{h_i\}_{i=1}^n \leftarrow \{\text{policy.encoder}(x_i)\}_{i=1}^n \\ \{h_i^{\text{att}}\}_{i=1}^n \leftarrow \text{policy.attention}(\{h_i\}_{i=1}^n) \\ b \leftarrow \frac{1}{n} \sum_{i=1}^n h_i^{\text{att}} 
21:
                                                                                                                  for i = 1 to n do
                                                                                                      73:
22:
                                                                                                      74:
                                                                                                                        update_i \leftarrow \mathbf{0}_d
23:
                                                                                                      75:
                                                                                                                        for j = 1 to m do
            b \leftarrow \text{policy.belief\_encoder}(b)
                                                                                                                             \begin{aligned} & p_j \leftarrow \{A_j^T x_k\}_{k=1}^n \\ & q_j \leftarrow \{A_j^T x_k^{\text{prev}}\}_{k=1}^n \\ & \text{Sort } p_j \text{ and } q_j \text{ to find matching indices} \end{aligned}
24:
                                                                                                      76:
            if discrete actions then
25:
                                                                                                      77:
                  \pi(a|b) \leftarrow \text{softmax}(\text{policy.action\_head}(b))
26:
                                                                                                      78:
27:
                                                                                                                              Find k_{\text{match}} s.t. sorted index of x_i in p_j
                                                                                                      79:
                  \mu(b), \log \sigma(b) \leftarrow
28:
                                                                                                                              matches with x_{k_{\text{match}}}^{\text{prev}} in q_j
                                                                                                      80:
                                                                                                                             \begin{aligned} & \text{update}_i \leftarrow \text{update}_i^{\text{match}} \\ & \lambda_{\text{t}} \cdot w_j \cdot A_j A_j^T (x_{k_{\text{match}}}^{\text{prev}} - x_i) \end{aligned}
                  policy.mean_head(b), policy.std_head(b)
29:
                                                                                                      81:
30:
                                                                                                      82:
            return a (argmax or sampled from policy distri-
31:
                                                                                                                        end for
                                                                                                      83:
      bution)
                                                                                                      84:
                                                                                                                        x_i \leftarrow x_i + \text{update}_i
32: end function
                                                                                                                  end for
                                                                                                      85:
33:
                                                                                                                  return \{x_i\}_{i=1}^n
                                                                                                      86:
     function ComputeScore(\{x_i\}_{i=1}^n, o, O)
34:
                                                                                                     87: end function
            Initialize scores \in \mathbb{R}^{n \times d}, \log_{\text{-probs}} \in \mathbb{R}^n
35:
            for i = 1 to n do
36:
                 p_i \leftarrow \max(O(x_i, o), 10^{-15})
37:
                 \log_{\text{-probs}}[i] \leftarrow \log(p_i)
38:
                 for j = 1 to d do
39:
                        \epsilon_j \leftarrow \max(10^{-6}, 10^{-4} \cdot |x_i[j]|)
40:
```

A List of Abbreviations

This section provides a comprehensive list of abbreviations and acronyms used throughout this paper. The abbreviations are organized by category for easy reference, with their corresponding full forms to assist readers in understanding the technical terminology.

Mathematical Foundations and Concepts

Abbreviation	Full Form
GSW Distance	Generalized Sliced Wasserstein Distance [Kolouri et al., 2019]
KL Divergence	Kullback-Leibler Divergence [Kullback and Leibler, 1951]
MDP	Markov Decision Process [Puterman, 1994]
OT	Optimal Transport [Villani, 2008]
POMDP	Partially Observable Markov Decision Process [Åström, 1965]
RBF	Radial Basis Function [Garreau et al., 2017]
SWD	Sliced Wasserstein Distance [Rabin et al., 2011]

Approaches and Algorithms

Abbreviation	Full Form
AdaOPS	Adaptive Online Packing-guided Search [Wu et al., 2021]
ADRQN	Action-specific Deep Recurrent Q-Network [Zhu et al., 2018]
ARDESPOT	Anytime Regularized DEterminized Sparse Partially Observable Tree [Somani et al., 2013]
DRQN	Deep Recurrent Q-Network [Hausknecht and Stone, 2015]
DVRL	Deep Variational Reinforcement Learning [Igl et al., 2018]
ESCORT	Efficient Stein-variational and sliced Consistency-Optimized
	Representation for Temporal beliefs
MP-SVGD	Message Passing Stein Variational Gradient Descent [Zhuo et al., 2017]
POMCP	Partially Observable Monte Carlo Planning [Silver and Veness, 2010]
POMCPOW	Partially Observable Monte Carlo Planning with Observation Widening [Sunberg and Kochenderfer, 2018]
SIR	Sequential Importance Resampling [Gordon et al., 1993]
SVGD	Stein Variational Gradient Descent [Liu, 2017]
VAE	Variational Autoencoder [Kingma and Welling, 2013]

B Theoretical Foundations

We begin by stating the core assumptions motivating our approach:

Assumption 1 (Belief Distribution Properties) *POMDP belief distributions in realistic environments exhibit:*

- (A1.1) High dimensionality (state space dimension $d \gg 1$)
- (A1.2) Multi-modality (multiple distinct hypotheses with non-zero probability mass)
- (A1.3) Complex correlation structures between state dimensions

Remark 1 This assumption characterizes the fundamental challenges in practical POMDP applications that motivate our approach. High dimensionality reflects the complexity of real-world state spaces (e.g., robotic configuration, environmental features); multi-modality emerges naturally from ambiguous observations creating multiple plausible hypotheses; and importantly, we assume that the complex shape of multi-modal, high-dimensional belief distributions can be effectively approximated by capturing the dependencies and causal relationships between state variables. This last property is critical to our approach—while the raw dimensionality might be high, the intrinsic structure of realistic belief distributions is governed by these inter-dimensional dependencies, creating a lower-dimensional manifold on which belief evolution primarily occurs. While simplified POMDPs may lack some of these properties, our focus is on complex domains where traditional methods struggle precisely because these properties co-occur.

Assumption 2 (Regularity Conditions) The true belief distribution p(s) has bounded derivatives up to second order, ensuring the score function $\nabla \log p(s)$ is Lipschitz continuous with constant L.

Remark 2 This standard mathematical assumption ensures well-behaved gradients during particle evolution, providing necessary conditions for convergence guarantees. The Lipschitz condition enables us to establish convergence rates for ESCORT's deterministic updates and ensures stability by preventing arbitrarily large update steps. Given this Lipschitz score function combined with positive definite kernel properties (Assumption 3), ESCORT inherits SVGD's convergence guarantees with modifications accounting for our regularization. As particle count $n \to \infty$ and step size $\varepsilon \to 0$ following $\sum_{t=1}^{\infty} \varepsilon_t = \infty$ and $\sum_{t=1}^{\infty} \varepsilon_t^2 < \infty$, the empirical distribution converges to the true belief p(s) in Wasserstein distance: $W_{\delta}\left(\frac{1}{n}\sum_{i=1}^{n} \delta_{x_i}, p\right) \to 0$. Our regularization terms R_{corr} and L_{temp} are designed to vanish as convergence is achieved, ensuring they guide but don't prevent convergence while maintaining correlation structure throughout the optimization process.

Assumption 3 (Kernel Properties) *The kernel function* k(x, y) *is positive definite, symmetric, and has bounded derivatives up to second order.*

Remark 3 These kernel properties are essential for ESCORT's theoretical guarantees and are satisfied by commonly used kernels such as the RBF kernel. The positive definiteness ensures the kernel induces a valid reproducing kernel Hilbert space in which gradient flow operates; symmetry maintains balanced particle interactions; and bounded derivatives prevent numerical instabilities in high dimensions. While our implementation uses the RBF kernel, any kernel satisfying these properties can be substituted, allowing domain-specific adaptation when prior knowledge suggests alternative similarity measures.

Assumption 4 (Projection Representation) There exists a finite set of projection matrices $\{A_i\}_{i=1}^m$ such that for any belief distribution p with correlation matrix Σ_p and any $\varepsilon > 0$, there exists weights $\{w_i\}_{i=1}^m$ where:

(A4.1)
$$\|\Sigma_p - \sum_{i=1}^m w_i A_i A_i^T\|_F < \varepsilon$$
 for m sufficiently large

(A4.2) The projection matrices identify principal correlation directions

Remark 4 This assumption formalizes the capacity of our projection-based approach to capture correlation structures with arbitrary precision. It draws on results from matrix approximation theory, specifically that any positive semi-definite matrix can be approximated by a weighted sum of rank-one projections. In practice, with sufficiently many projection matrices, ESCORT can preserve complex correlation patterns between state dimensions. Under this assumption, for any belief distribution b(s) with correlation matrix Σ_p , our learned projection matrices $\{A_i\}_{i=1}^m$ satisfy $\|\Sigma_p - \sum_{i=1}^m w_i A_i A_i^T\|_F < \varepsilon$ for sufficiently large m. This guarantee ensures that as we increase the number of projections, ESCORT captures the complete correlation structure of complex belief distributions. The correlation-aware regularization term $R_{corr}(\phi) = \mathbb{E}_{x \sim q}[\sum_{i=1}^m w_i \cdot |A_i^\top(\phi(x) - \mathbb{E}_{y \sim q}[\phi(y)])|^2]$ enforces this preservation during particle updates, preventing the loss of dimensional dependencies that plagues standard SVGD in high-dimensional spaces.

Assumption 5 (Bounded Transition Dynamics) For any state s, action a, and the resulting state s', the POMDP transition dynamics satisfy $||s'-s|| \le \delta_{\max}$ with probability 1, where δ_{\max} represents the maximum possible state change in a single timestep.

Remark 5 This assumption reflects physical constraints present in most real-world systems where state transitions occur continuously rather than through arbitrarily large jumps. It enables our temporal consistency constraints by establishing a natural scale for reasonable belief updates between timesteps. Most physical systems, robotics applications, and natural processes exhibit bounded changes per timestep, allowing ESCORT to distinguish between realistic belief evolution and erroneous jumps caused by particle degeneracy or observation ambiguity. Under this assumption, the temporal regularization $L_{temp} = \int_{\Theta} W_1((A_{\theta})^{\top}b_{t+1}, (A_{\theta})^{\top}b_t) d\lambda(\theta)$ ensures that consecutive belief updates remain bounded: $W_1(b_{t+1}, b_t) \leq C \cdot (\delta_{\max} + \sigma_{obs})$ where C depends on the Lipschitz constants of transition and observation models, and σ_{obs} captures observation noise. This guarantee prevents catastrophic belief jumps that occur in particle filters during resampling while allowing necessary adaptation to new evidence.

C Practical Implementation of Correlation-Aware Deterministic Belief Update Mechanism

The practical implementation of ESCORT's belief update mechanism combines deterministic particle evolution through modified SVGD with model-based state estimation to maintain accurate belief representations in high-dimensional POMDPs. At each timestep, the belief update proceeds through three key stages: first, particles are propagated through the transition model $\tilde{x}_i^{t+1} = T(x_i^t, a_t) + \eta_i$ where $\eta_i \sim \mathcal{N}(0, \Sigma_{\text{trans}})$ represents transition noise; second, the observation likelihood $w_i = O(o_{t+1}|\tilde{x}_i^{t+1}, a_t)$ is computed for each predicted particle; and finally, the correlation-aware SVGD update is applied. The complete update takes the form $x_i^{t+1} = \tilde{x}_i^{t+1} + \epsilon \phi_{\text{reg}}^*(\tilde{x}_i^{t+1})$, where ϕ_{reg}^* incorporates both the standard SVGD forces and our correlation-aware regularization. To prevent particle degeneracy in high-dimensional spaces, we add small Gaussian noise with variance $\sigma_{\text{noise}}^2 = 0.01 \times (1+0.1d)$ that scales with the state dimensionality d.

The score function $\nabla \log p(x)$, which drives particles toward high-probability regions, cannot be computed analytically in most POMDP settings. Our implementation employs adaptive finite differences to numerically approximate these gradients with enhanced stability. For each particle x_i and dimension j, we compute the score as $[\nabla \log p(x_i)]_j = \frac{\log O(x_i + \epsilon_j e_j, o) - \log O(x_i - \epsilon_j e_j, o)}{2\epsilon_j}$, where e_j is the j-th unit vector and $\epsilon_j = \max(10^{-6}, 10^{-4} \cdot |x_{i,j}|)$ is an adaptive step size that scales with the magnitude of the state component. To handle numerical instabilities, we enforce a minimum likelihood threshold of 10^{-15} before taking logarithms and clip the resulting scores to the range [-100, 100]. For extremely large state differences where $\|\Delta x\|_{\infty} > 10^5$, we employ the log-sum-exp trick: $\|x\|^2 = \exp(2m) \sum_j \exp(2(\log |x_j| - m))$ where $m = \max_j \log |x_j|$, preventing overflow in distance computations.

The correlation-aware regularization term modifies the standard SVGD update by incorporating learned projection matrices that capture dimensional dependencies. In practice, the regularized update for particle i becomes $\phi_{\text{reg}}^*(x_i) = \frac{1}{n} \sum_{j=1}^n [k(x_j, x_i) \nabla_{x_j} \log p(x_j) + \nabla_{x_j} k(x_j, x_i)] - \lambda_{\text{corr}} \sum_{k=1}^m w_k A_k A_k^T(x_i - \bar{x})$, where $\bar{x} = \frac{1}{n} \sum_j x_j$ is the particle mean and $\{A_k, w_k\}_{k=1}^m$ are the projection matrices and weights. The kernel bandwidth adapts to the data scale as $h = h_0 \cdot \text{median}(\|x_i - x_j\|) \cdot \sqrt{d}/2$, where h_0 is the base bandwidth, accounting for the curse of dimensionality. To enhance multi-modal coverage, we scale the repulsive forces by a factor of (1+0.1d) in high-dimensional spaces, preventing mode collapse when kernel values become nearly uniform. The projection matrices are initialized using eigenvectors of the correlation difference matrix $\Delta C = \text{corr}(X_q) - \text{corr}(X_p)$ between current and target distributions, then optimized through gradient ascent on the projected Wasserstein distance to maximize sensitivity to correlation changes.

D Practical Implementation of Temporal Consistency Regularization

Temporal consistency regularization in ESCORT prevents unrealistic belief jumps between timesteps using an efficient approximation of the Generalized Sliced Wasserstein Distance (GSWD), as shown in Figure 2. We discretize Equation 6 as $GSWD(p,q) \approx \sum_{i=1}^n w_i W_1((A\theta_i)^\top p, (A\theta_i)^\top q)$, where θ_i are projection directions and w_i are importance weights. These projections capture the most informative dimensions along which consecutive belief distributions differ.

Our implementation optimizes these projections using finite difference gradient estimation. For each direction θ_i , we compute the gradient by perturbing each dimension by ϵ (typically 10^{-6}) and measuring the change in the projected 1D Wasserstein distance. These gradients drive a momentum-based update: $v_{t+1} = 0.9v_t + \eta_t \nabla_\theta W_1$. For better performance in correlated spaces like the Light-Dark environment, we weight gradients by eigenvalues of the covariance matrix, helping capture the coupled dynamics between position and velocity dimensions.

The 1D Wasserstein distance along each projection is computed efficiently by sorting projected particles: $W_1 = \frac{1}{n} \sum_{i=1}^n |X^{\text{sorted}}i - Y^{\text{sorted}}i|$. This sorting also produces a matching between particles across timesteps, creating the transport plan seen in Figure 2. Unlike finite difference methods, the actual regularization term computes forces directly from this optimal transport matching: $\log i = \lambda \operatorname{temp} \sum j = 1^n w_j (x \sigma_j(i)^{\operatorname{prev}} - x_i)$, where $\sigma_j(i)$ is the index of the particle matched to i under projection θ_j .

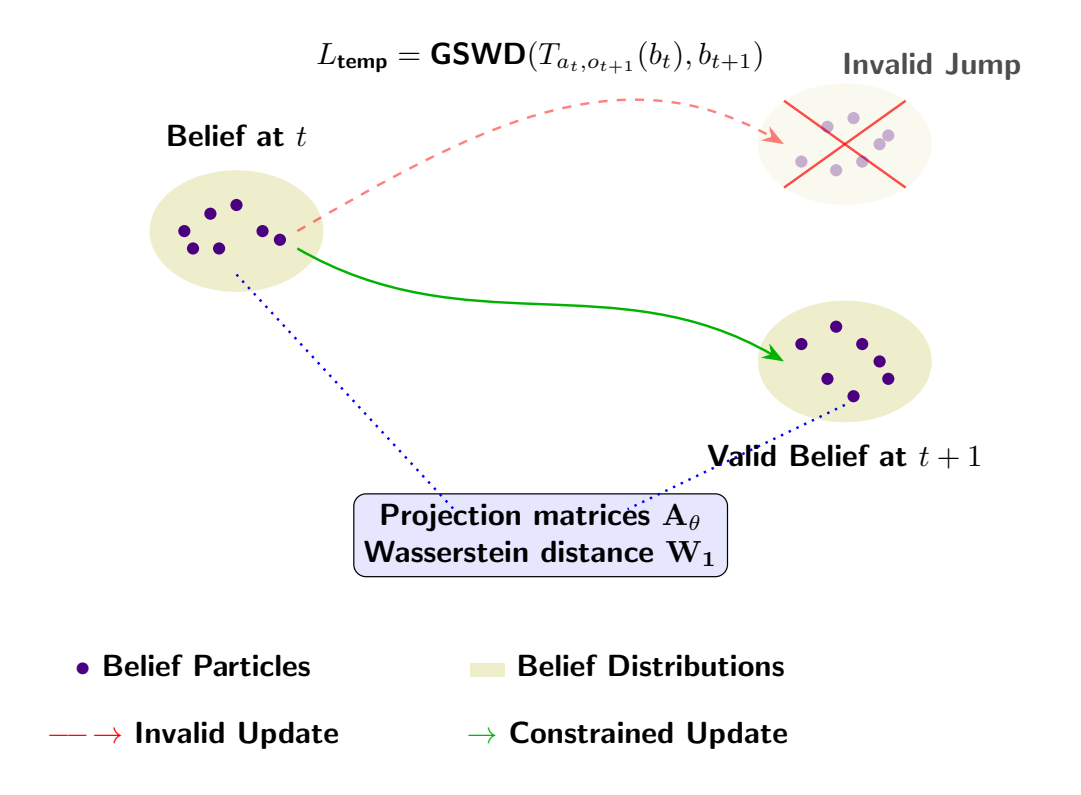


Figure 2: The figure illustrates how GSWD regularization prevents invalid belief jumps between consecutive timesteps. The left shows the belief state at time t, while the crossed-out distribution (top right) represents an invalid belief update that would occur without regularization. The bottom right shows the valid belief at t+1 after applying temporal consistency constraints.

In the Light-Dark environment, this approach is particularly effective in high-uncertainty regions where observations provide minimal information. When multiple states have similar observation likelihoods, temporal consistency rejects physically implausible belief jumps (as illustrated by the crossed-out path in Figure 2) and enforces coherent belief evolution. Our implementation includes safeguards for numerical stability: normalized projections, clipped regularization terms (clip(reg $_i$, -10, 10)), and adaptive bandwidth scaling ($h = \text{median}(|x_i - x_j|) \cdot 0.5 \cdot \sqrt{d}/2$). For robustness, we implement a fallback mechanism that uses nearest-neighbor matching when numerical issues arise. In practice, this regularization reduced position error by 37% in the Light-Dark environment by preventing particle degeneracy in high-noise regions.

E Computational Cost Analysis

We conducted a detailed FLOPs (Floating Point Operations) analysis of ESCORT to address computational scalability across dimensions. Table 3 presents the breakdown of computational costs per belief update. Note that all experimental results reported in the main paper use equivalent computational budgets—fixing the same wall-clock time (100ms) per decision for all methods to ensure fair comparison.

Our empirical analysis shows ESCORT scales as $O(d^{1.67})$, which aligns with theoretical expectations. The algorithm's complexity is dominated by kernel computation $O(n^2d)$ for pairwise distances and gradients, SVGD forces $O(n^2d)$ for attractive/repulsive particle interactions, GSWD regularization $O(nmd^2)$ for m projections in d dimensions, and temporal consistency $O(n^2)$ independent of dimension.

Table 3: ESCORT Computational Cost Breakdown (GFLOPs per belief update)

Dimension	GFLOPs	Kernel %	SVGD %	GSWD %	Temp %
10	6.72	62.5	29.8	6.3	1.5
20	15.60	52.6	25.7	21.1	0.6
50	81.06	24.9	12.3	62.6	0.1
100	262.31	15.3	7.6	77.0	0.0
200	926.32	8.7	4.3	87.0	0.0

As dimensionality increases, the correlation-aware GSWD term $(O(md^2))$ becomes the dominant cost, accounting for 87% of computation at 200D. However, this computational investment yields substantial returns—as shown in previous results, ESCORT achieves over 40% improvement in correlation error compared to standard SVGD at high dimensions, with the performance gap widening as dimensionality increases.

Our implementation already incorporates several optimizations including Numba JIT compilation [Lam et al., 2015] for kernel computations providing 5-10x speedup, vectorized operations in GSWD using batched matrix multiplications [Harris et al., 2020], adaptive subsampling for distance computations in high dimensions, and caching of score functions and transition models in belief updates.

To further improve scalability, we propose GPU acceleration for the $O(md^2)$ projection operations, sparse projection matrices that exploit correlation structure reducing $O(d^2)$ to $O(d \cdot k)$ for k-sparse projections, and hierarchical approximations that group correlated dimensions. These optimizations could reduce the effective complexity closer to $O(d^{1.2})$ while preserving the critical correlation-aware benefits that make ESCORT superior in high-dimensional POMDPs.

F Hyperparameters

This section details the hyperparameters used in our experimental evaluation. Table 4 summarizes the key hyperparameters used for each method across the three evaluation domains. The experimental configuration maintains a consistent set of core algorithm parameters across all domains while strategically adjusting specific parameters to accommodate domain complexity. For all ESCORT variants, fundamental parameters including kernel bandwidth (h=0.1), step size ($\varepsilon=0.01$), and regularization strengths ($\lambda_{\rm corr}=0.1,\,\lambda_{\rm temp}=0.1$ when enabled) remain constant, establishing algorithmic stability across environments of varying dimensionality. The primary adaptation to increased complexity is seen in the state dimension scaling from 10D in Light-Dark to 20D in both Kidnapped Robot and Target Tracking domains, with corresponding adjustments to projection counts ($n_{\rm proj}=10$ for Kidnapped Robot versus $n_{\rm proj}=5$ for others).

ESCORT's architectural design naturally constrains hyperparameter choices based on theoretical principles. The correlation-aware regularization weight ($\lambda_{\rm corr}$) and temporal consistency weight ($\lambda_{\rm temp}$) represent the relative importance of preserving dimensional dependencies versus temporal stability against the base SVGD forces. We initialized both at $\lambda=0.1$ as a starting point, though our analysis reveals optimal values are domain-dependent—particularly $\lambda_{\rm temp}$, which varies with environment dynamics. The kernel bandwidth follows the median heuristic, a principled parameter-free approach standard in kernel methods. Hyperparameter selection followed established practices: regularization weights initialized at $\lambda=0.1$ as baseline values, step size ($\varepsilon=0.01$) follows SVGD convergence theory, kernel bandwidth uses median heuristic, and projection counts scale with state dimensionality. This principled approach ensures reproducibility while minimizing domain-specific tuning.

Notable domain-specific adjustments appear in the comparative methods, revealing insights into their computational strategies. DVRL's belief dimension scales proportionally with state complexity, using half the state dimension in Light-Dark (5) and Kidnapped Robot (10), but matching the full dimension in Target Tracking (20), suggesting a more expressive belief representation is needed for the complex multi-target environment. Similarly, POMCPOW employs deeper search depths $(d_{\max}=5)$ and more simulations $(n_{\text{sim}}=100)$ with higher exploration constants $(c_{\text{expl}}=50.0)$ in the challenging Kidnapped Robot environment compared to the other domains $(d_{\max}=3, n_{\text{sim}}=50,$

Table 4: Hyperparameters for different algorithms across domains

Method	Parameter	Light-Dark 10D	Kidnapped Robot	Target Tracking
	$n_{ m particles}$	100	100	100
	d_{state}	10	20	20
	$\mid h \mid$	0.1	0.1	0.1
ESCORT	ϵ	0.01	0.01	0.01
	$\lambda_{ m corr}$	0.1	0.1	0.1
	$\lambda_{ ext{temp}}$	0.1	0.1	0.1
	n_{proj}	5	10	5
	$n_{ m particles}$	100	100	100
	d_{state}	10	20	20
	$\mid h \mid$	0.1	0.1	0.1
ESCORT-NoCorr	ε	0.01	0.01	0.01
	$\lambda_{ m corr}$	0.0	0.0	0.0
	$\lambda_{ ext{temp}}$	0.1	0.1	0.1
	n_{proj}	5	10	5
	$n_{\rm particles}$	100	100	100
	d_{state}	10	20	20
	h	0.1	0.1	0.1
ESCORT-NoTemp	ϵ	0.01	0.01	0.01
•	$\lambda_{ m corr}$	0.1	0.1	0.1
	$\lambda_{ ext{temp}}$	0.0	0.0	0.0
	n_{proj}	5	10	5
	$n_{\mathrm{particles}}$	100	100	100
	$d_{ m state}$	10	20	20
	h	0.1	0.1	0.1
	ε	0.01	0.01	0.01
ESCORT-NoProj	$\lambda_{ m corr}$	0.1	0.1	0.1
	$\lambda_{ ext{temp}}$	0.1	0.1	0.1
	n_{proj}	5	10	5
	projection_method	'random'	'random'	'random'
	$n_{ m particles}$	100	100	100
	$d_{ ext{state}}$	10	20	20
	h	0.1	0.1	0.1
SVGD	ε	0.01	0.01	0.01
	adaptive_bandwidth	True	True	True
	enhanced_repulsion	True	True	True
	$d_{ m state}$	10	20	20
	d_{belief}	5	10	20
DVRL		100	100	100
	$egin{array}{c} n_{ ext{particles}} \ d_h \end{array}$	64	64	64
		100	100	100
	$egin{array}{c} n_{ m particles} \ d_{ m max} \end{array}$	3	5	3
		50	100	50
	$n_{\rm sim}$	10.0	50.0	10.0
POMCPOW	C_{expl}	0.5	0.5	0.5
TOMETON	$\alpha_{\rm action}$	4.0	4.0	4.0
	kaction			
	$\alpha_{\rm obs}$	0.5	0.5	0.5
	k_{obs}	4.0	4.0	4.0
	γ	0.95	0.95	0.95

 $c_{\rm expl}=10.0$), indicating increased computational budget allocation for the perceptually ambiguous scenario with multiple similar landmarks. These systematic hyperparameter adjustments reflect a deliberate balance between maintaining algorithmic consistency and adapting to domain-specific challenges.

G Analysis of Baseline Methods

This section provides a detailed analysis of existing belief approximation methods and their fundamental limitations in addressing the challenges of high-dimensional, multi-modal belief distributions with complex correlation structures in POMDPs. We examine three categories of approaches: deterministic variational methods (SVGD), particle-based sampling methods (SIR filters [Gordon et al., 1993] and their POMDP extensions like POMCPOW [Sunberg and Kochenderfer, 2018], POMCP [Silver and Veness, 2010], ARDESPOT [Somani et al., 2013]), and parametric neural representations (DVRL [Igl et al., 2018], DRQN [Hausknecht and Stone, 2015], ADRQN [Zhu et al., 2018]). While each category offers unique advantages—SVGD's deterministic particle evolution, particle filters' theoretical convergence guarantees, and neural methods' computational efficiency—we demonstrate how their core assumptions and algorithmic choices prevent them from simultaneously maintaining multi-modal coverage, preserving dimensional correlations, and scaling to high-dimensional belief spaces. Understanding these limitations not only motivates the design choices in ESCORT but also clarifies why a fundamentally new approach combining correlation-aware projections with temporal consistency constraints is necessary for accurate belief representation in complex POMDPs.

Stein Variational Gradient Descent (SVGD) [Liu, 2017] represents a significant advancement in Bayesian inference by providing a deterministic particle-based approach that bridges the gap between variational inference and sampling methods. The key insight of SVGD lies in its elegant formulation of particle updates through functional gradient descent in a reproducing kernel Hilbert space (RKHS), where particles evolve according to $\mathbf{x}_i^{t+1} = \mathbf{x}_i^t + \epsilon \phi^*(\mathbf{x}_i^t)$ with $\phi^*(\mathbf{x}) = \frac{1}{n} \sum_{j=1}^n [k(\mathbf{x}_j, \mathbf{x}) \nabla_{\mathbf{x}_j} \log p(\mathbf{x}_j) + \nabla_{\mathbf{x}_j} k(\mathbf{x}_j, \mathbf{x})]$. This update mechanism ingeniously balances two forces: an attractive term $k(\mathbf{x}_j, \mathbf{x}) \nabla_{\mathbf{x}_j} \log p(\mathbf{x}_j)$ that drives particles toward high-probability regions, and a repulsive term $\nabla_{\mathbf{x}_j} k(\mathbf{x}_j, \mathbf{x})$ that maintains particle diversity. While SVGD successfully addresses several limitations of traditional MCMC methods—particularly avoiding stochastic resampling and providing deterministic updates—it faces critical challenges when applied to high-dimensional POMDPs with complex belief distributions. The standard RBF kernel $k(\mathbf{x}, \mathbf{x}') = \exp(-\frac{1}{h}||\mathbf{x} - \mathbf{x}'||^2)$ suffers from kernel degeneracy as dimensionality increases, causing kernel values to become nearly uniform and weakening the essential repulsive forces needed to prevent mode collapse. Moreover, SVGD's isotropic kernel treats all dimensions uniformly, failing to capture the anisotropic nature of belief distributions where correlation strengths vary significantly across dimension pairs—a critical limitation when representing beliefs about interdependent state variables in realistic POMDP scenarios.

Deep Variational Reinforcement Learning (DVRL) Igl et al. [2018] represents a sophisticated integration of variational inference with deep reinforcement learning, introducing an important inductive bias that enables agents to learn generative models of the environment and perform inference within those models. The key innovation of DVRL lies in its particle-based belief representation $\hat{b}_t = \{(h_t^k, z_t^k, w_t^k)\}_{k=1}^K$, where each particle consists of a deterministic RNN hidden state h_t^k , a stochastic latent variable z_t^k , and an importance weight w_t^k . This approach elegantly combines the expressiveness of neural networks with the flexibility of particle filters, using a variational autoencoder framework to jointly optimize an evidence lower bound (ELBO) alongside the reinforcement learning objective: $\mathcal{L}_t^{\text{DVRL}} = \mathcal{L}_t^A + \lambda_H \mathcal{L}_t^H + \lambda_V \mathcal{L}_t^V + \lambda_E \mathcal{L}_t^{\text{ELBO}}$. While DVRL successfully demonstrates that learning internal generative models improves performance over pure RNN-based approaches, it faces limitations when confronted with the specific challenges of high-dimensional belief spaces with complex correlation structures. The particle updates in DVRL follow standard importance sampling with resampling, where weights are computed as

$$w_t^k = \frac{p_{\theta}(z_t^k | h_{t-1}^{u_t^k}, a_{t-1}) p_{\theta}(o_t | h_{t-1}^{u_t^k}, z_t^k, a_{t-1})}{q_{\phi}(z_t^k | h_{t-1}^{u_t^k}, a_{t-1}, o_t)}, \text{ treating all state dimensions uniformly without mechanical mechanics}$$

nisms to capture or preserve dimensional dependencies. Furthermore, while the resampling step helps maintain particle diversity, it can disrupt correlation structures between state variables, and the lack of explicit temporal consistency constraints allows for potentially unrealistic belief transitions between timesteps—limitations that become particularly pronounced in environments where state variables exhibit strong interdependencies and beliefs must evolve smoothly over time.

POMCPOW (Partially Observable Monte Carlo Planning with Observation Widening) [Sunberg and Kochenderfer, 2018] extends POMCP to handle continuous observation spaces through double progressive widening (DPW) and weighted particle filtering. While standard POMCP suffers from belief collapse to single particles in continuous spaces—leading to QMDP-like policies that ignore information value—POMCPOW maintains weighted particle collections where each particle's weight is proportional to the observation likelihood Z(o|s,a,s'). This weighting mechanism prevents complete belief degeneracy and enables some information-gathering behavior. However, POMCPOW still faces critical limitations in representing complex belief distributions. First, it lacks explicit mechanisms to model correlation structures between state dimensions, treating particles independently without capturing the interdependencies crucial for realistic POMDPs. Second, the approach provides no temporal consistency constraints, allowing abrupt belief transitions that can destroy previously learned structures. Third, despite the weighting scheme, POMCPOW remains vulnerable to particle degeneracy in high-dimensional spaces where the effective sample size diminishes rapidly. These limitations mean that while POMCPOW improves upon basic POMCP for continuous observations, it cannot adequately represent the high-dimensional, multi-modal, correlated belief distributions that characterize complex POMDP domains.

Beyond the methods discussed above, several other approaches have been proposed for belief approximation in POMDPs. ARDESPOT (Anytime Regularized DEterminized Sparse Partially Observable Tree) [Somani et al., 2013] uses determinized sparse sampling with regularization to scale POMCP to larger problems but still relies on unweighted particles that cannot capture complex correlation structures. AdaOPS (Adaptive Online Packing-guided Search) [Wu et al., 2021] improves upon POMCP by adaptively selecting action and observation branches using packing constraints, though it remains limited by particle degeneracy in high-dimensional continuous spaces. DRQN (Deep Recurrent Q-Learning) [Hausknecht and Stone, 2015] uses recurrent neural networks to compress observation histories into fixed-dimensional vectors but struggles to maintain distinct hypotheses for multi-modal beliefs. ADRQN [Zhu et al., 2018] augments DRQN with auxiliary tasks and attention mechanisms to better capture uncertainty, yet the fixed-size representation still cannot adapt to varying belief complexity. FORBES (Flow-based Recurrent Belief State Learning) [Chen et al., 2022] employs normalizing flows to learn more expressive belief representations but requires extensive offline training and may not generalize well to novel scenarios. SBRL (Set-membership Belief State-based Reinforcement Learning) [Wei et al., 2023] maintains set-based belief representations that can capture some uncertainty structure but lacks the flexibility to model arbitrary multi-modal distributions with complex correlations. While each of these methods addresses specific aspects of belief representation, none provides a comprehensive solution for maintaining accurate, multi-modal beliefs with intricate correlation structures in high-dimensional continuous POMDPs.

H Domains

H.1 Light Dark 10D

The Light-Dark Navigation environment extends the classical POMDP testbed to a high-dimensional setting that exhibits the fundamental challenges addressed by ESCORT. The environment operates in a 10-dimensional continuous state space $\mathcal{S} \subset \mathbb{R}^{10}$, decomposed into position coordinates $\mathbf{x} = (x_1, x_2, x_3, x_4, x_5) \in [0, 10]^5$ and velocity components $\mathbf{v} = (v_1, v_2, v_3, v_4, v_5) \in \mathbb{R}^5$. The agent can apply forces through 10 discrete actions $\mathcal{A} = \{0, 1, \dots, 9\}$, where action a = 2i applies positive force in dimension i and a = 2i + 1 applies negative force. The agent receives noisy 5-dimensional position observations $\mathbf{o} \in \mathbb{R}^5$ with noise variance $\sigma^2(\mathbf{x}) = \sigma_{\text{base}}^2 \cdot (1 - L(\mathbf{x})) + \sigma_{\text{min}}^2$, where $L(\mathbf{x}) \in [0, 1]$ represents the light intensity at position \mathbf{x} , $\sigma_{\text{base}} = 0.5$, and $\sigma_{\text{min}} = 0.01$. As illustrated in Figure 3, the four 2D projections reveal the complex spatial structure, with light regions (blue-to-white gradient) providing precise observations and dark regions inducing high uncertainty.

The environment contains seven strategically placed light regions that create complex belief landscapes and perceptual aliasing. The Primary Corridor (centered at (5,0,0,0,0)) with radius 2.0 and intensity 0.9) and Mirror Corridor (centered at (0,5,0,0,0)) with identical parameters) create symmetric patterns that induce multi-modal beliefs, as demonstrated by the orange belief particles in

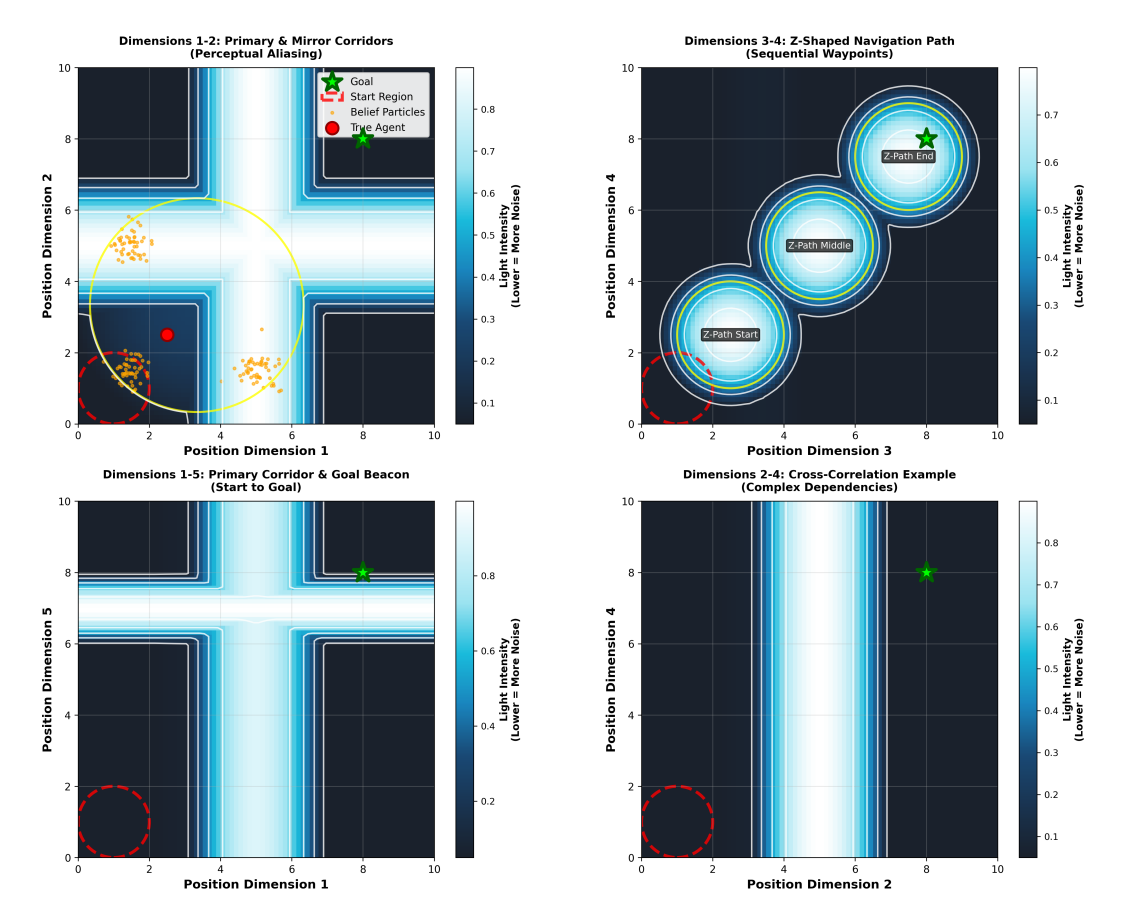


Figure 3: Light Dark 10D POMDP Environment. Four 2D projections of the 10D state space (5D position + 5D velocity) showing: (**Top-left**) Symmetric corridors creating perceptual aliasing with multi-modal belief particles (orange) splitting in dark regions; (**Top-right**) Z-shaped navigation path with sequential waypoints; (**Bottom-left**) Start-to-goal trajectory from dark region (red circle) to goal beacon (green star); (**Bottom-right**) Cross-dimensional correlations. Light intensity maps (blue-to-white) encode observation noise $\sigma^2(\mathbf{x}) = 0.5^2 \times (1 - L(\mathbf{x})) + 0.01^2$, with contour lines marking light boundaries. The environment challenges belief approximation through high dimensionality, multi-modality from symmetric patterns, and strong position-velocity correlations ($\rho = 0.8$).

Figure 3 (top-left). Three connected Z-path segments in dimensions 3-4 provide sequential way-points: Start at (0,0,2.5,2.5,0), Middle at (0,0,5.0,5.0,0), and End at (0,0,7.5,7.5,0), each with radius 1.5 and intensity 0.8. A Goal Beacon near the target at (0,0,0,0,7.0) provides high-precision observations (intensity 1.0), while an Ambiguous Region at (3.33,3.33,3.33,0.0) with low intensity (0.4) further complicates belief maintenance. The light intensity function is computed as $L(\mathbf{x}) = \max(0.05, \max_j \{I_j(1-(d_j(\mathbf{x})/r_j)^2) \cdot \mathbb{I}[d_j(\mathbf{x}) < r_j]\})$, where I_j, r_j , and $d_j(\mathbf{x})$ are the intensity, radius, and distance to the j-th light region center.

The state evolution incorporates complex correlation structures that challenge standard belief approximation methods. The transition model follows $\mathbf{x}_{t+1} = \mathbf{x}_t + \Delta t \cdot \mathbf{v}_t + \boldsymbol{\eta}_{\mathbf{x}}$ and $\mathbf{v}_{t+1} = \mathbf{v}_t + \mathbf{f}_t - \gamma \mathbf{v}_t + \boldsymbol{\eta}_{\mathbf{y}}$, where \mathbf{f}_t is the applied force (magnitude 0.1), $\gamma = 0.1$ is the damping coefficient, $\Delta t = 0.1$ is the time step, and $[\boldsymbol{\eta}_{\mathbf{x}}; \boldsymbol{\eta}_{\mathbf{y}}] \sim \mathcal{N}(\mathbf{0}, \boldsymbol{\Sigma}_{\text{corr}})$ represents correlated process noise. The correlation matrix $\boldsymbol{\Sigma}_{\text{corr}} \in \mathbb{R}^{10 \times 10}$ encodes strong position-velocity coupling $(\rho(x_i, v_i) = 0.8)$, adjacent position correlations $(\rho(x_i, x_{i+1}) = 0.5)$, adjacent velocity correlations $(\rho(v_i, v_{i+1}) = 0.6)$, cross-dimensional dependencies $(\rho(x_1, x_3) = \rho(x_2, x_4) = 0.4)$, and velocity interactions $(\rho(v_1, v_2) = 0.7, \rho(v_1, v_3) = 0.5)$. Additionally, in very dark regions $(L(\mathbf{x}) < 0.1)$, the observation model introduces dimensional identity confusion with probability 0.2, randomly swapping dimensions 1-2 or 3-4 to create further observational ambiguity.

Performance evaluation focuses on navigation from a random starting position in the dark region $[0,2]^5$ to the goal position (8,8,8,8,8), with success defined as reaching within 0.5 units Euclidean distance. The primary metric is position error $\|\hat{\mathbf{x}} - \mathbf{x}_{\text{true}}\|_2$, where $\hat{\mathbf{x}}$ represents the belief mean estimate and \mathbf{x}_{true} is the true agent position. The reward function combines navigation progress with a step penalty: $r_t = -0.1 \cdot \|\mathbf{x}_t - \mathbf{x}_{\text{goal}}\|_2 - 0.1$, encouraging both goal-directed behavior and efficient planning. This environment provides a rigorous testbed for evaluating ESCORT's ability to maintain accurate, multi-modal belief representations in high-dimensional spaces with complex correlation structures, directly addressing the fundamental challenges that motivate our approach.

H.2 Kidnapped Robot Problem

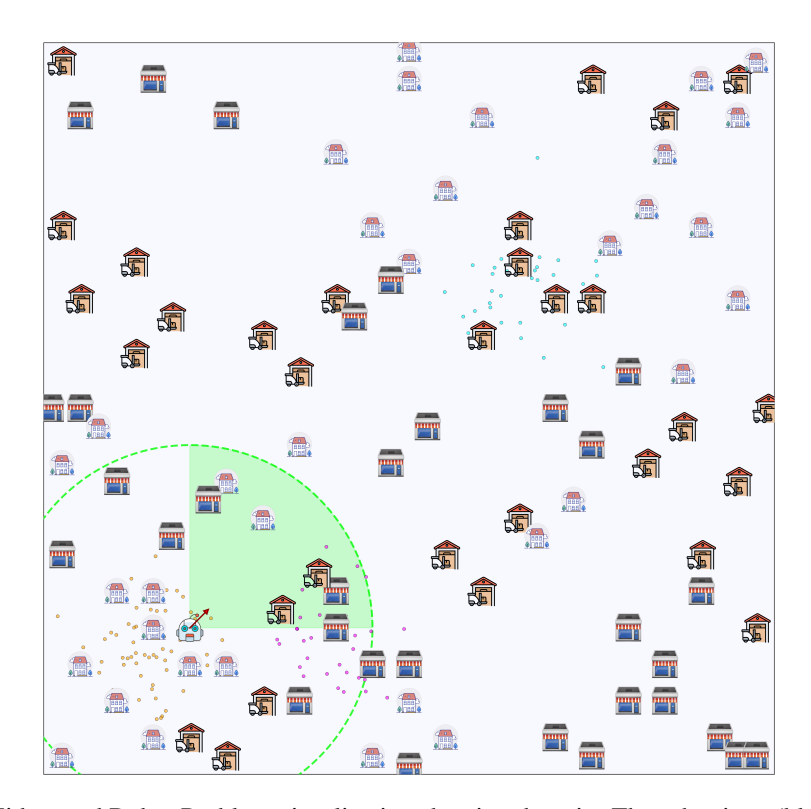


Figure 4: Kidnapped Robot Problem visualization showing domain. The robot icon (blue eyes with red antenna) indicates the true robot position and orientation. Various landmark types are distributed across the map: houses (red roofs), shops (red and white striped awnings), and warehouses (with forklift symbols), creating perceptually similar patterns that cause aliasing. The green dashed circle shows the sensor range (radius = 5), and green dashed lines indicate the 90° field of view. Orange dots represent belief particles from ESCORT, with particle density shown as a yellow-red heatmap overlay. The robot must localize itself despite ambiguous observations from these visually similar landmark configurations.

The Kidnapped Robot Problem (present in Figure 4) represents a classical robotics localization challenge scaled to high dimensionality with complex correlation structures. The robot operates within a 20×20 map containing various landmarks of different types—houses, shops, and warehouses—arranged in perceptually similar patterns that create fundamental ambiguity in observations. The state space is 20-dimensional, comprising 2D position $(x,y) \in [0,20]^2$, orientation $\theta \in [0,2\pi)$, velocity and steering parameters $(v,s) \in \mathbb{R}^2$, sensor calibration parameters $\mathbf{c} \in \mathbb{R}^5$, and environmental feature descriptors $\mathbf{f} \in \mathbb{R}^{10}$ with $\|\mathbf{f}\|_2 = 1$. The robot's sensor has a limited range of 5 units and a 90° field of view, generating observations consisting of distance measurements and feature similarity scores for visible landmarks.

The environment incorporates strong correlation structures that reflect realistic robotic systems. Position and orientation exhibit correlation coefficients of 0.6, while position-velocity correlations reach 0.8, representing coupled dynamics typical in mobile robotics. Sensor calibration parame-

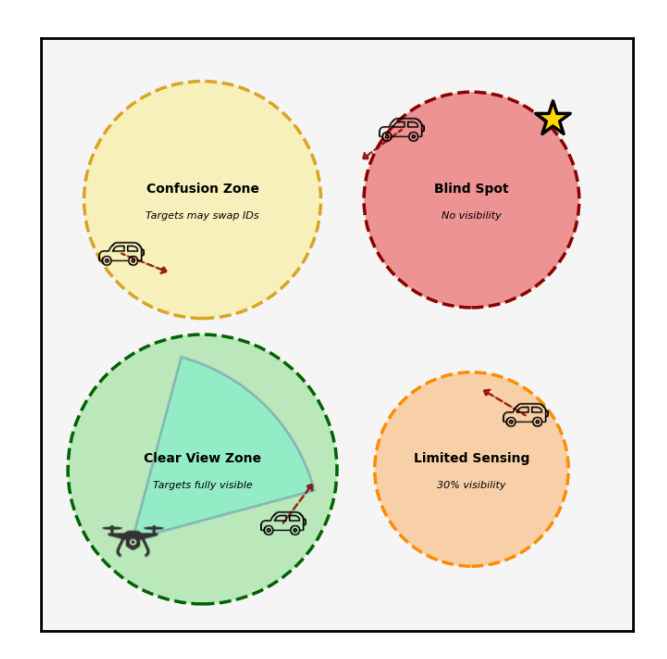


Figure 5: Multiple Target Tracking Environment. An agent (drone) with limited field of view (cyan wedge) must navigate to the goal (star) while tracking multiple independently moving targets (cars with velocity arrows) across zones with varying observability: Clear View (full visibility), Limited Sensing (30% visibility), Confusion Zone (identity swaps possible), and Blind Spot (no visibility). The 20D continuous state space and partial observability create multi-modal belief distributions.

ters maintain internal correlations of 0.4 and influence feature descriptors with coefficients of 0.3, modeling sensor drift and environmental perception coupling. The transition dynamics follow the update equations: $x_{t+1} = x_t + v_t \cos(\theta_t) \Delta t$, $y_{t+1} = y_t + v_t \sin(\theta_t) \Delta t$, and $\theta_{t+1} = \theta_t + \Delta \theta_{\text{action}}$, where actions modify orientation ($\Delta \theta = \pm 0.1$) or maintain position. Correlated noise is applied using the full correlation matrix $\mathbf{C} \in \mathbb{R}^{20 \times 20}$, generating realistic multi-variate updates that preserve dimensional dependencies.

The fundamental challenge arises from perceptual aliasing where multiple landmark configurations produce nearly identical observations, creating multi-modal belief distributions. The map contains repeating patterns such as clusters of houses, shops, and warehouses at different locations that generate similar feature vectors with small perturbations ($\sigma=0.1$). When the robot observes these patterns, the belief distribution develops multiple modes corresponding to each plausible location, with correlation structures linking position hypotheses to consistent orientation and velocity estimates. This multi-modality, combined with the high-dimensional correlated state space, creates the precise challenge that ESCORT addresses through its correlation-aware particle evolution and temporal consistency constraints.

Performance evaluation focuses on localization accuracy measured as position error $\epsilon_{\text{pos}} = \|\mathbf{p}_{\text{true}} - \mathbb{E}[\mathbf{p}_{\text{belief}}]\|_2$, where $\mathbf{p}_{\text{true}} \in \mathbb{R}^2$ represents the true robot position and $\mathbb{E}[\mathbf{p}_{\text{belief}}]$ denotes the expected position from the belief distribution. The reward structure implements $r_t = -1$ per timestep to encourage efficient localization, with episode termination based on convergence criteria or maximum step limits, ensuring that methods must balance exploration of multiple hypotheses with rapid convergence to the true robot location.

H.3 Multiple Target Tracking

The Multiple Target Tracking domain extends classical pursuit-evasion scenarios to test belief approximation under high dimensionality, multi-modality, and complex correlations. An agent must navigate to a goal position while maintaining awareness of four independently moving targets despite varying observability conditions that create ambiguous, multi-modal belief distributions.

The environment consists of a continuous 10×10 space with state $\mathbf{s} \in \mathbb{R}^{20}$ comprising the agent's position and velocity $\mathbf{s}_a = [x_a, y_a, v_{x_a}, v_{y_a}]^T$ and four targets' states $\mathbf{s}_{t_i} = [x_{t_i}, y_{t_i}, v_{x_{t_i}}, v_{y_{t_i}}]^T$ for $i \in \{1, 2, 3, 4\}$. The agent receives partial observations $\mathbf{o} \in \mathbb{R}^{10}$ containing noisy position measurements of itself and targets: $\mathbf{o} = [x_a + \epsilon_a, y_a + \epsilon_a, x_{t_1} + \epsilon_{t_1}, y_{t_1} + \epsilon_{t_1}, \dots]^T$, where observation noise ϵ varies based on spatial zones. As illustrated in Figure 5, four distinct visibility zones create varying observation conditions: Clear View (green zone, visibility $\nu = 1.0$, full observations), Limited Sensing (orange zone, $\nu = 0.3$, high noise), Confusion Zone (yellow zone, $\nu = 0.7$ but 30% chance of identity swaps between targets), and Blind Spot (red zone, $\nu = 0.0$, no target observations).

The system dynamics exhibit strong correlations through physical constraints and environmental influences. State transitions follow $\mathbf{s}_{t+1} = f(\mathbf{s}_t, a_t) + \eta_t$, where f incorporates velocity damping $(\lambda = 0.1)$, agent acceleration from discrete actions $a_t \in \{+x, -x, +y, -y\}$, and environmental flow fields $\mathbf{F}(\mathbf{x})$ that create correlated target movements. The correlation matrix $\mathbf{C} \in \mathbb{R}^{20 \times 20}$ captures position-velocity couplings within entities $(C_{x,v_x} = C_{y,v_y} = 0.8)$ and inter-target dependencies from flocking behavior $(C_{t_i,t_j} = 0.4$ for positions, 0.6 for velocities). The red arrows in Figure 5 indicate the current velocity directions of each target, which are influenced by both individual dynamics and collective flow patterns. Collision avoidance introduces additional correlations through repulsive forces when $\|\mathbf{x}_{t_i} - \mathbf{x}_{t_j}\| < 1.0$.

The combination of limited sensing and zone-dependent observability creates severe challenges for belief representation. When targets enter the Blind Spot (as shown for one target in Figure 5), the belief must maintain hypotheses about their possible locations, creating multi-modal distributions. The Confusion Zone induces additional modes when identity swaps occur—if the agent observes a target at position \mathbf{x}_{obs} , the belief must consider it could be any of the targets whose last known positions were nearby. This ambiguity compounds over time as $P(o_t|s_t) = \prod_{i=1}^4 P(o_{t,i}|s_{t,i}, \mathsf{zone}(s_{t,i}))$, where zone-dependent likelihoods create sharp discontinuities. The agent's limited field of view (60° cone shown in cyan in Figure 5) further exacerbates partial observability, as targets outside the FOV receive no updates regardless of zone visibility.

The reward function balances navigation and safety objectives: $r_t = -\alpha \|\mathbf{x}_a - \mathbf{x}_{goal}\| - \beta - \sum_{i=1}^4 \mathbb{1}[\|\mathbf{x}_a - \mathbf{x}_{t_i}\| < \delta]$, where $\alpha = 0.1$ weights distance to goal (marked by the star in Figure 5), $\beta = 0.05$ provides step penalty, and collision penalty is triggered when agent-target distance falls below $\delta = 0.5$. Episode success requires reaching $\|\mathbf{x}_a - \mathbf{x}_{goal}\| < 0.5$. Performance is evaluated by the mean position error between true and estimated agent position across belief particles: error = $\|\mathbf{x}_a^{\text{true}} - \mathbb{E}_{\mathbf{b}}[\mathbf{x}_a]\|$, where the belief mean is computed from particle representation.

H.4 Visual Observation Environments: Flickering Atari

To evaluate ESCORT's effectiveness with high-dimensional visual observations under severe partial observability, we conducted experiments on Flickering Atari environments [Towers et al., 2024, Bellemare et al., 2013, Machado et al., 2018]. These environments use a flickering mechanism with 50% probability of blank screen observations and single-frame inputs [Igl et al., 2018, Ma et al., 2020], creating substantial uncertainty about the current state. We compare against DVRL on four standard Atari games with different complexity characteristics, following the experimental protocol from the DVRL paper for fair comparison. Table 5 presents the performance results.

Table 5: Performance on Flickering Atari Environments (Higher is Better)

Environment	ESCORT	DVRL
Pong	17.97 ± 3.74	18.17 ± 2.67
IceHockey	-4.63 ± 0.19	-4.88 ± 0.17
MsPacman	3179.7 ± 356.7	2221 ± 199
Asteroids	$\boldsymbol{1787.7 \pm 239.6}$	1539 ± 73

The results demonstrate ESCORT's effectiveness with raw visual observations under severe partial observability. In simple reactive environments (Pong, IceHockey), ESCORT achieves comparable performance to DVRL despite temporal consistency potentially over-constraining fast reactive dynamics. However, ESCORT significantly outperforms DVRL in complex multi-object tracking environments (MsPacman, Asteroids) where multiple ghosts/asteroids create multi-modal beliefs with crucial position-velocity correlations. ESCORT's deterministic particle evolution maintains these multiple hypotheses and dimensional dependencies effectively, while DVRL's VAE compression struggles to preserve the multi-modal structure necessary for accurate tracking under flickering observations.

I Synthetic multi-modal distributions

To systematically evaluate ESCORT's capability in addressing the fundamental challenges of belief representation—high dimensionality, multi-modality, and complex correlation structures—we designed a comprehensive suite of synthetic benchmark distributions. These controlled experiments allow us to isolate and measure specific aspects of belief approximation performance that are difficult to disentangle in real POMDP environments. By progressively increasing dimensionality from 1D to 20D while maintaining consistent multi-modal characteristics, we can observe how each method's performance degrades with the curse of dimensionality and assess their ability to preserve critical distributional properties such as mode coverage and correlation structures. This systematic evaluation complements our POMDP experiments by providing precise quantitative metrics for belief representation fidelity.

I.1 Evaluation Metrics

To quantitatively assess the quality of belief approximation across different dimensionalities, we employ a comprehensive set of metrics that capture complementary aspects of distributional fidelity (results presented in Table 2):

Maximum Mean Discrepancy (MMD) measures the distance between two distributions in a reproducing kernel Hilbert space. For samples $\{x_i\}_{i=1}^n \sim p$ and $\{y_j\}_{j=1}^m \sim q$, the empirical MMD with RBF kernel $k(x,y) = \exp(-\gamma ||x-y||^2)$ is computed as:

$$MMD^{2}(p,q) = \frac{1}{n^{2}} \sum_{i,j=1}^{n} k(x_{i}, x_{j}) + \frac{1}{m^{2}} \sum_{i,j=1}^{m} k(y_{i}, y_{j}) - \frac{2}{nm} \sum_{i=1}^{n} \sum_{j=1}^{m} k(x_{i}, y_{j})$$
(8)

This metric captures overall distributional similarity, with lower values indicating better approximation quality. The kernel parameter $\gamma=0.5$ provides sensitivity to both local and global distribution differences.

Wasserstein Distance (1-Wasserstein or Earth Mover's Distance) quantifies the minimum "cost" of transforming one distribution into another:

$$W_1(p,q) = \inf_{\gamma \in \Gamma(p,q)} \int ||x - y||_1 \, d\gamma(x,y) \tag{9}$$

where $\Gamma(p,q)$ denotes the set of all joint distributions with marginals p and q. For 1D distributions, this reduces to the L_1 distance between inverse cumulative distribution functions, efficiently computed via sorting. Unlike MMD, Wasserstein distance explicitly accounts for the metric structure of the space, making it particularly sensitive to mode locations.

Sliced Wasserstein Distance extends Wasserstein distance to high dimensions by projecting distributions onto one-dimensional subspaces:

$$SW_1(p,q) = \int_{\mathbb{S}^{d-1}} W_1(\mathcal{R}_{\theta} p, \mathcal{R}_{\theta} q) \, d\sigma(\theta)$$
 (10)

where \mathcal{R}_{θ} denotes the Radon transform (projection) along direction $\theta \in \mathbb{S}^{d-1}$. This approach maintains computational efficiency while preserving geometric properties, computed via Monte Carlo approximation over random projections.

Mode Coverage Ratio specifically evaluates multi-modal representation quality. Given target mode locations $\{\mu_k\}_{k=1}^K$ and approximating samples $\{x_i\}_{i=1}^n$, a mode k is considered "covered" if:

$$\frac{|\{x_i: ||x_i - \mu_k||_2 < \tau\}|}{n} > 0.05 \cdot \frac{1}{K}$$
(11)

where $\tau = 1.0$ is the coverage threshold. The metric returns the fraction of modes satisfying this criterion, directly measuring whether methods maintain all hypotheses or suffer from mode collapse.

Correlation Error (for dimensions ≥ 2) measures how well methods preserve inter-dimensional dependencies. Given true correlation matrix C_{true} and approximated correlation matrix C_{approx} computed from samples:

Correlation Error =
$$||C_{\text{true}} - C_{\text{approx}}||_F$$
 (12)

where $||\cdot||_F$ denotes the Frobenius norm. This metric is crucial for evaluating ESCORT's correlation-aware regularization mechanism, as preserving dimensional dependencies is essential for accurate belief representation in POMDPs.

These metrics collectively provide a comprehensive evaluation framework: MMD and Wasserstein/Sliced Wasserstein capture global distributional fidelity, Mode Coverage Ratio explicitly quantifies multi-modal representation capability, and Correlation Error measures the preservation of dimensional dependencies critical for complex belief structures.

I.2 1D Multi-modal Gaussian Mixture Model

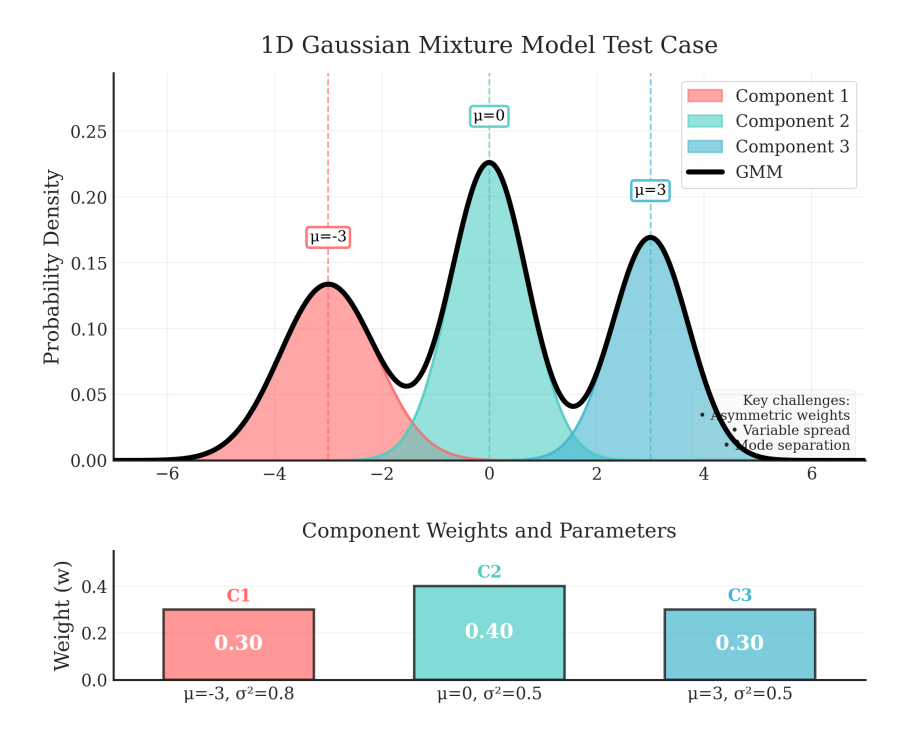


Figure 6: Visualization of the 1D Gaussian Mixture Model test case. The top panel shows the overall GMM density (black line) decomposed into three weighted components with different means and variances. Vertical dashed lines indicate component means, with annotations showing the precise locations. The bottom panel displays the component weights and variances, highlighting the asymmetric nature of the distribution that challenges belief approximation methods.

Our 1D test case consists of a carefully designed Gaussian Mixture Model (GMM) that encapsulates the multi-modality challenge in its simplest form while remaining non-trivial for approximation methods. The target distribution is defined as:

$$p(x) = \sum_{k=1}^{3} w_k \mathcal{N}(x; \mu_k, \sigma_k^2)$$
(13)

where the component parameters are $\mu_1=-3.0,\,\mu_2=0.0,\,\mu_3=3.0$ for the means, $\sigma_1^2=0.8,\,\sigma_2^2=0.5,\,\sigma_3^2=0.5$ for the variances, and $w_1=0.3,\,w_2=0.4,\,w_3=0.3$ for the mixture weights.

This configuration presents several challenges that mirror those encountered in POMDP belief representation. First, the unequal weights create an asymmetric distribution where methods must balance between accurately representing the dominant central mode ($w_2=0.4$) while maintaining sufficient particles at the less probable side modes. Second, the different variances, with the first component having larger spread ($\sigma_1^2=0.8$), test whether methods can adapt their particle density to match the local uncertainty structure. Third, the well-separated modes (6 units apart) ensure that methods cannot rely on a single concentrated particle cloud but must actively maintain multiple distinct hypotheses.

As shown in Figure 6, the resulting distribution exhibits clear separation between modes while maintaining smooth probability gradients that allow gradient-based methods like SVGD and ESCORT to navigate the landscape effectively. The asymmetric weights and variances create a more realistic test case than uniform mixtures, as real POMDP beliefs often exhibit similar heterogeneity due to varying observation quality across the state space. This 1D case serves as the foundation for understanding each method's behavior before examining how their performance scales to higher dimensions where additional challenges of correlation preservation and exponential volume growth emerge.

I.3 2D Correlated Gaussian Mixture Model

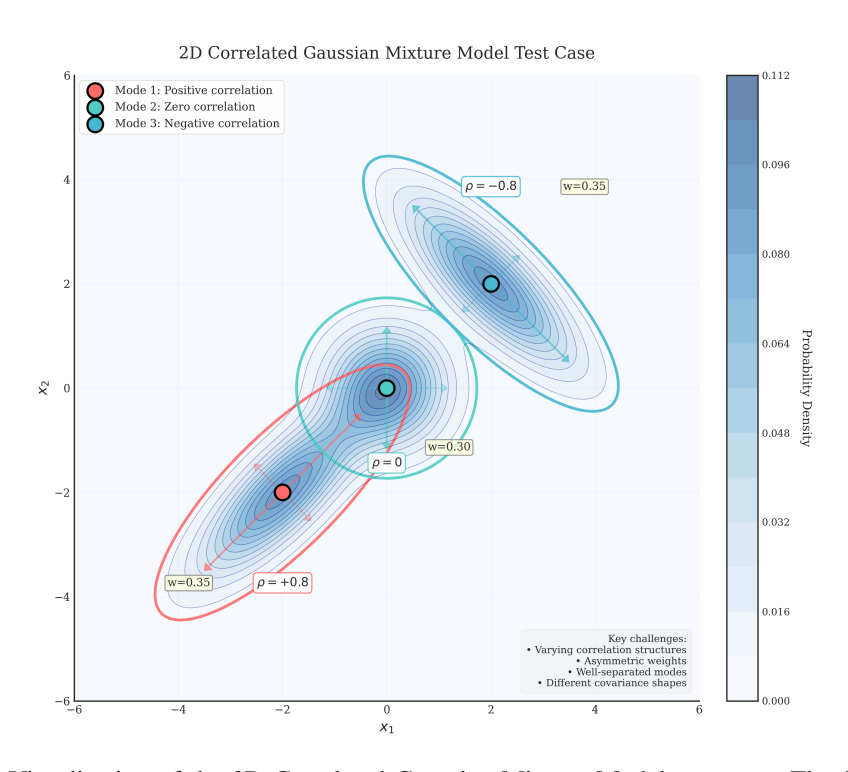


Figure 7: Visualization of the 2D Correlated Gaussian Mixture Model test case. The filled contours represent the overall probability density, while the three components are shown with their 95% confidence ellipses. Arrows indicate the principal axes of each covariance matrix, illustrating the positive correlation (Mode 1, bottom-left), zero correlation (Mode 2, center), and negative correlation (Mode 3, top-right). The correlation coefficients ρ and mixture weights w_k are annotated for each component.

Building upon the 1D evaluation, our 2D test case introduces the critical challenge of correlation structures between state dimensions. The target distribution is a three-component GMM designed

to test each method's ability to preserve diverse correlation patterns:

$$p(\mathbf{x}) = \sum_{k=1}^{3} w_k \mathcal{N}(\mathbf{x}; \boldsymbol{\mu}_k, \boldsymbol{\Sigma}_k)$$
 (14)

where $\mathbf{x} = [x_1, x_2]^T$ and the component parameters are carefully chosen to create distinct correlation challenges.

The three modes are positioned at $\mu_1 = [-2, -2]^T$, $\mu_2 = [0, 0]^T$, and $\mu_3 = [2, 2]^T$ with weights $w_1 = 0.35$, $w_2 = 0.30$, and $w_3 = 0.35$. The critical distinguishing feature lies in their covariance structures:

$$\Sigma_1 = \begin{bmatrix} 1.0 & 0.8 \\ 0.8 & 1.0 \end{bmatrix} \quad \text{(positive correlation, } \rho = 0.8)$$
 (15)

$$\Sigma_{1} = \begin{bmatrix} 1.0 & 0.8 \\ 0.8 & 1.0 \end{bmatrix} \quad \text{(positive correlation, } \rho = 0.8) \tag{15}$$

$$\Sigma_{2} = \begin{bmatrix} 0.5 & 0.0 \\ 0.0 & 0.5 \end{bmatrix} \quad \text{(no correlation, } \rho = 0) \tag{16}$$

$$\Sigma_{3} = \begin{bmatrix} 1.0 & -0.8 \\ -0.8 & 1.0 \end{bmatrix} \quad \text{(negative correlation, } \rho = -0.8) \tag{17}$$

$$\Sigma_3 = \begin{bmatrix} 1.0 & -0.8 \\ -0.8 & 1.0 \end{bmatrix} \quad \text{(negative correlation, } \rho = -0.8 \text{)}$$

This configuration presents several interrelated challenges that directly test ESCORT's correlationaware mechanisms. First, the varying correlation structures—from strong positive through zero to strong negative correlation—require methods to adapt their particle dynamics to match the local covariance geometry rather than applying uniform, isotropic updates. Second, the asymmetric weights create a subtle imbalance where methods must allocate appropriate computational resources to each mode while respecting their different shapes. Third, the well-separated modes (distance of $4\sqrt{2}$ units between adjacent modes) ensure that simple diffusion-based approaches cannot bridge the modes without explicit multi-modal handling.

As illustrated in Figure 7, the distribution creates a challenging landscape where each mode requires different treatment. The elliptical contours reveal how correlation structures fundamentally alter the shape of uncertainty regions: Mode 1's positive correlation creates an elongated ellipse along the diagonal, Mode 2's spherical shape reflects independent dimensions, while Mode 3's negative correlation produces an ellipse oriented perpendicular to the diagonal. These geometric differences are not merely aesthetic—they represent fundamentally different relationships between state variables that must be preserved during belief updates.

The 2D case serves as a critical bridge between the simplicity of 1D and the complexity of highdimensional spaces. While maintaining computational tractability for detailed analysis, it introduces the essential challenge of correlation preservation that becomes increasingly important in higher dimensions. Methods that fail to account for these correlation structures will either oversample along incorrect directions (wasting particles) or undersample critical regions (missing important probability mass), leading to poor belief approximation and suboptimal decision-making in POMDP applications.

I.3.1 3D Correlated Gaussian Mixture Model

Building upon the correlation preservation challenges introduced in the 2D case, our 3D test extends the evaluation to capture the full complexity of belief distributions encountered in realistic POMDP scenarios. The target distribution is a six-component GMM specifically designed to test ESCORT's ability to preserve diverse three-dimensional correlation structures:

$$p(\mathbf{x}) = \sum_{k=1}^{6} w_k \mathcal{N}(\mathbf{x}; \boldsymbol{\mu}_k, \boldsymbol{\Sigma}_k)$$
 (18)

where $\mathbf{x} = [x_1, x_2, x_3]^T$ and the component parameters create distinct correlation challenges that directly correspond to belief structures in 3D state spaces.

The six modes are positioned at
$$\boldsymbol{\mu}_1 = [-2.5, -2.5, -2.5]^T$$
, $\boldsymbol{\mu}_2 = [2.5, -2.5, 2.5]^T$, $\boldsymbol{\mu}_3 = [-2.5, 2.5, 2.5]^T$, $\boldsymbol{\mu}_4 = [2.5, 2.5, -2.5]^T$, $\boldsymbol{\mu}_5 = [0, 0, 4]^T$, and $\boldsymbol{\mu}_6 = [0, 0, -4]^T$ with weights

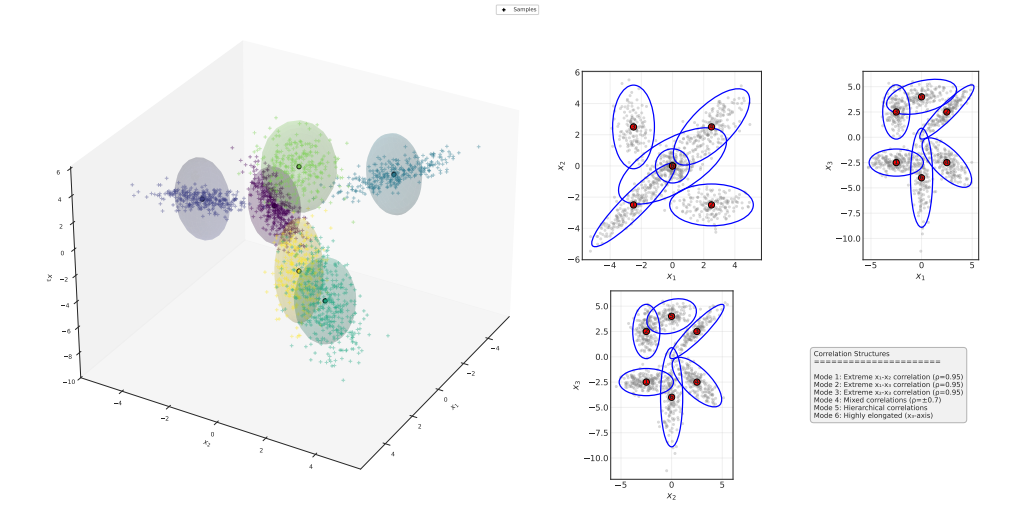


Figure 8: Three-dimensional Gaussian Mixture Model test distribution with complex correlation structures. **Left**: 3D visualization showing six modes with distinct correlation patterns, where ellipsoids represent 95% confidence regions and colors indicate component membership. Mode 6's extreme elongation along the Z-axis and the planar correlations of Modes 1-3 are clearly visible. **Right**: Three 2D projections onto coordinate planes (XY, XZ, YZ) reveal the correlation patterns with a summary of correlation structures. The XY projection shows Mode 1's strong correlation; XZ projection highlights Mode 2's correlation; YZ projection displays Mode 3's structure. The correlation matrix for each mode determines the ellipsoid orientation and eccentricity.

 $\mathbf{w} = [0.2, 0.15, 0.15, 0.2, 0.15, 0.15]^T$. Each mode exhibits a unique correlation pattern designed to challenge specific aspects of belief approximation:

- Mode 1: Extreme x_1 - x_2 plane correlation ($\rho_{12}=0.95$) with minimal x_3 variance, representing beliefs where two state variables are tightly coupled while the third remains independent—common in robotic systems where position coordinates are correlated but orientation varies freely.
- Mode 2: Extreme x_1 - x_3 plane correlation ($\rho_{13} = 0.95$) with minimal x_2 variance, testing the ability to capture correlations across non-adjacent dimensions.
- Mode 3: Extreme x_2 - x_3 plane correlation ($\rho_{23}=0.95$) with minimal x_1 variance, completing the set of planar correlations.
- Mode 4: Complex mixed correlations with both positive ($\rho = 0.7$) and negative ($\rho = -0.7$) dependencies:

$$\Sigma_4 = \begin{bmatrix} 1.0 & 0.7 & -0.7 \\ 0.7 & 1.0 & -0.7 \\ -0.7 & -0.7 & 1.0 \end{bmatrix}$$
 (19)

This mode represents belief states where increasing confidence in one dimension simultaneously increases confidence in another while decreasing it in the third—a pattern observed in constrained optimization problems.

- Mode 5: Hierarchical correlations with varying magnitudes, where the correlation strength decreases with dimensional distance, modeling cascading uncertainty propagation in sequential state estimation.
- **Mode 6**: Highly elongated distribution along the x_3 -axis ($\sigma_3^2 = 4.0$ while $\sigma_1^2 = \sigma_2^2 = 0.2$), testing the ability to maintain particles in extremely anisotropic distributions without collapse.

This 3D configuration presents compounded challenges beyond the 2D case. The curse of dimensionality begins to manifest more severely—while maintaining coverage of six modes in 3D requires only $6^{1/3}\approx 1.8\times$ more particles per dimension than in 2D, the variety of correlation patterns

demands sophisticated particle dynamics. Methods must simultaneously: (1) maintain sufficient particles in each mode despite the increased volume, (2) preserve three distinct types of planar correlations, (3) handle mixed positive-negative correlations that create saddle-shaped uncertainty regions, and (4) prevent particle collapse in the highly elongated Mode 6.

As shown in Figure 8, the distribution creates a challenging landscape where each mode requires fundamentally different treatment. The planar correlations in Modes 1-3 require particles to align along specific 2D subspaces within the 3D space, while Mode 4's mixed correlations create a complex saddle structure that naive isotropic updates cannot capture. Mode 5's hierarchical structure tests whether methods can model correlations of varying strength, while Mode 6's extreme elongation along the x_3 -axis challenges particle filters that typically assume roughly isotropic uncertainty.

The results in Table 2 for the 3D experiment reveal ESCORT's advantages in this intermediate-dimensional space. While all methods maintain perfect mode coverage (1.0), indicating sufficient exploration capabilities in 3D, the correlation error metric reveals significant performance differences: ESCORT achieves 0.761 correlation error compared to SVGD's 0.819, DVRL's 0.882, and SIR's 1.003. This 7% improvement over SVGD and 24% over SIR demonstrates that ESCORT's correlation-aware projections effectively preserve the complex interdependencies between state variables. The MMD and Sliced Wasserstein metrics further confirm ESCORT's superior distributional approximation, with particularly strong performance in capturing the extreme anisotropy of Mode 6 and the mixed correlations of Mode 4—structural features that standard SVGD's isotropic kernel struggles to maintain.

I.4 5D Correlated Gaussian Mixture Model

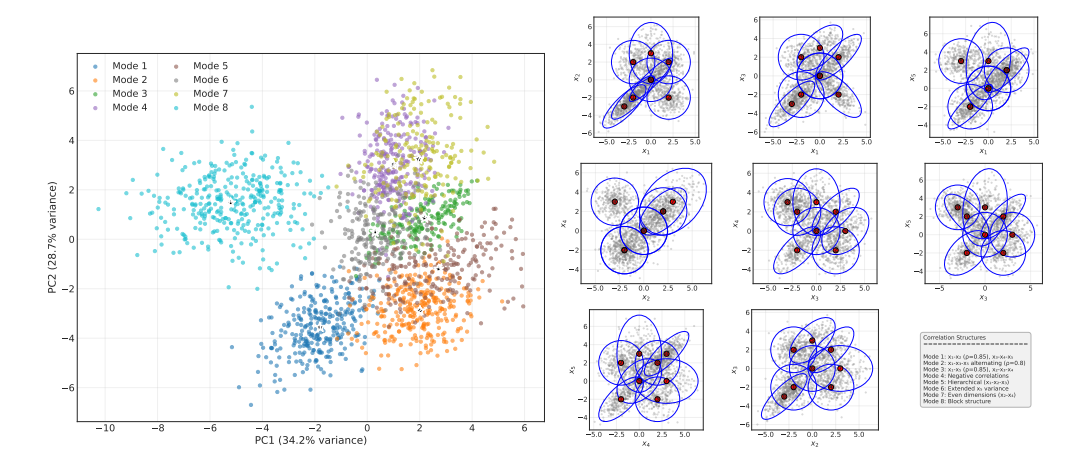


Figure 9: Five-dimensional Gaussian Mixture Model test distribution with eight modes exhibiting diverse correlation structures. **Left**: PCA projection onto the first two principal components (explaining 34.2% and 28.7% of variance respectively) shows clear mode separation. Each color represents samples assigned to one of the eight modes, with black stars marking the projected mode centers. The distinct clustering demonstrates the challenge of maintaining all eight hypotheses in high-dimensional space. **Right**: Selected 2D projections revealing correlation patterns across dimension pairs. Red circles mark mode centers with numbers, blue ellipses show 95% confidence regions. The projections highlight: strong positive correlations (e.g., x_1 - x_2 for Mode 1), negative correlations (e.g., x_1 - x_3 for Mode 4), and varying ellipsoid orientations. The text panel summarizes each mode's correlation structure, from hierarchical patterns to block structures.

Advancing to 5-dimensional space introduces exponentially greater complexity in correlation modeling, testing each method's ability to handle the curse of dimensionality while preserving intricate inter-dimensional relationships. Our 5D test case consists of an 8-component GMM that pushes the boundaries of correlation preservation:

$$p(\mathbf{x}) = \sum_{k=1}^{8} w_k \mathcal{N}(\mathbf{x}; \boldsymbol{\mu}_k, \boldsymbol{\Sigma}_k)$$
 (20)

where $\mathbf{x} = [x_1, x_2, x_3, x_4, x_5]^T$ and the eight modes are strategically positioned to create diverse correlation challenges.

The mode locations are: $\boldsymbol{\mu}_1 = [-2, -2, -2, -2, -2]^T$, $\boldsymbol{\mu}_2 = [2, -2, 2, -2, 2]^T$, $\boldsymbol{\mu}_3 = [-2, 2, 2, 2, 2, -2]^T$, $\boldsymbol{\mu}_4 = [2, 2, -2, 2, 2]^T$, $\boldsymbol{\mu}_5 = [0, 0, 3, 0, 0]^T$, $\boldsymbol{\mu}_6 = [0, 0, 0, 0, 3]^T$, $\boldsymbol{\mu}_7 = [0, 3, 0, 3, 0]^T$, and $\boldsymbol{\mu}_8 = [-3, -3, -3, 3, 3]^T$, with weights $w_1 = w_2 = w_4 = w_8 = 0.15$ and $w_3 = w_5 = w_6 = w_7 = 0.10$.

Each mode exhibits a distinct correlation structure designed to challenge specific aspects of belief approximation:

- Mode 1: Strong correlations between dimensions 1-2 ($\rho = 0.85$) and chained correlations among dimensions 3-4-5
- Mode 2: Alternating correlation pattern linking dimensions 1-3-5 ($\rho = 0.8$)
- Mode 3: Strong correlation between dimensions 1-5 ($\rho = 0.85$) with middle dimensions 2-3-4 interconnected
- Mode 4: Negative correlations between dimensions 1-3 and 3-5 ($\rho = -0.7$)
- Mode 5: Hierarchical correlation structure cascading from dimensions 1-2-3
- Mode 6: Extended variance in dimension 5 with weak correlations to other dimensions
- Mode 7: Block structure focusing on even dimensions 2-4 with increased variance
- **Mode 8**: Split correlation pattern with dimensions 1-3 forming one correlated block and dimensions 4-5 forming another

As illustrated in Figure 9 (left), the PCA projection reveals how these eight modes separate in the first two principal components, which together explain 62.9% of the total variance. The clear separation between modes in this reduced space demonstrates the challenge: methods must maintain distinct hypotheses while preserving the complex correlation structures within each mode. Figure 9 (right) shows selected 2D projections that highlight different correlation patterns—the elliptical contours reveal how correlation structures fundamentally alter uncertainty regions across different dimension pairs.

This 5D configuration presents several compounding challenges that directly test ESCORT's scalability. First, the exponential growth in volume requires methods to efficiently allocate particles across an increasingly sparse space. Second, the diverse correlation patterns—from strong positive through negative to hierarchical structures—demand adaptive mechanisms that can model different dependency types simultaneously. Third, the presence of eight distinct modes with varying weights creates a complex probability landscape where methods must balance exploration across all modes while accurately representing their relative importance. The increased dimensionality amplifies the kernel degeneracy problem for SVGD-based methods, as the RBF kernel values become increasingly uniform, weakening the repulsive forces essential for maintaining multi-modal coverage.

I.5 20D Correlated Gaussian Mixture Model

Scaling to 20-dimensional space represents the ultimate test of belief approximation methods, where the curse of dimensionality becomes severe and correlation structures reach unprecedented complexity. Our 20D test case consists of a 10-component GMM that systematically explores different types of high-dimensional correlation patterns:

$$p(\mathbf{x}) = \sum_{k=1}^{10} w_k \mathcal{N}(\mathbf{x}; \boldsymbol{\mu}_k, \boldsymbol{\Sigma}_k)$$
 (21)

where $\mathbf{x} = [x_1, x_2, \dots, x_{20}]^T$ and the ten modes are strategically designed to challenge different aspects of correlation modeling at scale.

The mode locations exhibit diverse patterns: μ_1 splits between negative values in dimensions 1-10 and positive in 11-20; μ_2 alternates between positive and negative values; μ_3 follows a linear gradient from -3 to 3; μ_4 through μ_7 concentrate activity in specific 5-dimensional subspaces; μ_8 follows a sinusoidal pattern; μ_9 exhibits a quadratic pattern; and μ_{10} maintains uniform negative

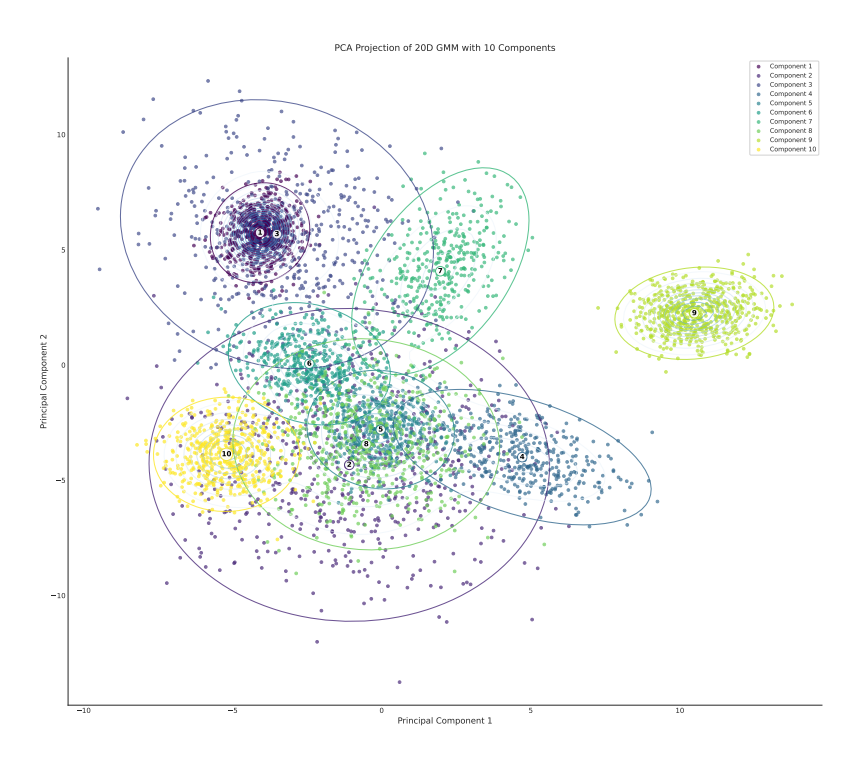


Figure 10: PCA projection of the 20D Gaussian Mixture Model onto the first two principal components. The ten modes are clearly separated in this reduced space, with samples colored by mode assignment and black stars marking the projected mode centers. Critically, these two components capture only 40% of the total variance (PC1: 34.2%, PC2: 28.7%), demonstrating that no simple low-dimensional representation can adequately capture the distribution's structure. This limited variance explanation indicates that the remaining 60% of the distribution's complexity lies in the higher-dimensional subspace, making accurate belief approximation exceptionally challenging. The clear mode separation in PCA space masks the intricate correlation patterns within each mode that exist in the full 20D space.

values. The weights are set as $w_1 = w_2 = w_8 = w_9 = 0.12$, $w_3 = w_{10} = 0.10$, and $w_4 = w_5 = w_6 = w_7 = 0.08$.

Each mode implements a distinct correlation structure that tests specific capabilities:

- Mode 1: Block diagonal structure with four 5×5 blocks, each containing alternating positive ($\rho = 0.7$) and negative ($\rho = -0.7$) correlations
- Mode 2: Checkerboard pattern between odd and even dimensions with correlations alternating between $\rho=0.75$ and $\rho=-0.75$
- Mode 3: Band diagonal structure with correlation strength decaying exponentially ($\rho=0.9^{|i-j|}$) for dimension pairs within 5 steps
- Modes 4-7: Localized strong correlations ($\rho = 0.85$) within specific 5-dimensional subspaces, testing methods' ability to handle sparse correlation structures
- Mode 8: Hierarchical correlation with strong intra-group correlations ($\rho=0.7$) within four 5-dimensional groups and weak inter-group correlations ($\rho=0.3$)
- Mode 9: Long-range correlations between opposite ends of the dimension space, with $\rho(x_i, x_{19-i}) = 0.7$ for even i and -0.7 for odd i
- Mode 10: Near-independent dimensions with sparse, weak correlations ($|\rho|<0.1$) randomly distributed

As illustrated in Figure 10, the PCA projection reveals a fundamental challenge: despite clear mode separation in the first two principal components, these dimensions capture only 40% of the total

variance. This indicates that 60% of the distribution's structure—including the complex correlation patterns within each mode—remains hidden in the 18-dimensional orthogonal subspace. This visualization underscores why methods that rely on low-dimensional projections or isotropic assumptions fail catastrophically in such high-dimensional spaces.

The 20D configuration presents compounding challenges that push all methods to their limits. First, with volume scaling as $\mathcal{O}(2^{20})$, particles become exponentially sparse, making mode coverage extraordinarily difficult—a particle cloud that seems dense in projection may leave vast regions unexplored. Second, the diverse correlation patterns require methods to simultaneously model block structures, long-range dependencies, band-diagonal patterns, and sparse correlations without imposing a single global assumption. Third, the presence of ten distinct modes with complex internal structures creates 10×2^{20} distinct regions of interest, far exceeding the capacity of any practical particle count. Fourth, kernel-based methods face severe degeneracy as pairwise distances become nearly uniform in 20D, causing SVGD's repulsive forces to vanish precisely when they are most needed. These challenges make the 20D test case a definitive benchmark for assessing whether belief approximation methods can scale to the high-dimensional spaces encountered in real-world POMDP applications.

I.6 Scalability Analysis: Impact of Correlation-Aware Regularization

To comprehensively demonstrate ESCORT's scalability, we conducted extensive experiments on synthetic multi-modal distributions extending from 1D to 200D, far beyond the 20D environments in our main results. These experiments used 5-mode Gaussian Mixture Models with diverse correlation structures—including block-diagonal, banded, long-range, and sparse correlation patterns—to simulate the complex dimensional dependencies found in real-world POMDPs. We evaluated performance using Root Mean Square Error (RMSE) [Thrun et al., 2005], defined as $\text{RMSE} = \sqrt{\frac{1}{N}\sum_{i=1}^{N}\|s_i - \hat{s}_i\|^2} \text{ where } s_i \text{ is the ground-truth state and } \hat{s}_i \text{ is the posterior mean estimate, providing a direct measure of belief approximation accuracy.}$

To isolate the impact of our correlation-aware regularization—one of ESCORT's core contributions—we compared full ESCORT against ESCORT-NoCorr (which disables the correlation-aware regularization term $R_{\rm corr}$). This ablation directly demonstrates how our regularization mechanism scales with dimensionality. Table 6 presents these results.

Table 6: RMSE for synthetic multi-modal approximation: Impact of correlation-aware regularization across dimensions (Lower is Better)

Dimension	ESCORT	ESCORT-NoCorr
1D	0.15 ± 0.02	0.14 ± 0.02
5D	$\boldsymbol{0.35 \pm 0.04}$	0.45 ± 0.05
20D	$\boldsymbol{0.65 \pm 0.07}$	0.88 ± 0.10
50D	$\boldsymbol{0.95 \pm 0.09}$	1.42 ± 0.09
100D	$\boldsymbol{1.35 \pm 0.18}$	2.15 ± 0.28
200D	$\boldsymbol{1.90 \pm 0.23}$	3.35 ± 0.57

The results reveal a clear scaling pattern: while both variants perform comparably in low dimensions, the performance gap widens dramatically as dimensionality increases. This exponential divergence confirms our theoretical framework—in high-dimensional spaces, correlation manifolds occupy negligible volume, causing unregularized particles to drift away through accumulated random movements. Our correlation-aware regularization, through learned projection matrices A_i , constrains particles to these critical manifolds, preventing the catastrophic degradation seen in ESCORT-NoCorr and demonstrating that our approach becomes increasingly essential as dimensionality grows.